SAND2007-6754C

Influence of Fuel Autoignition Reactivity on the High-Load Limits of HCCI Engines

Magnus Sjöberg and John E. Dec
Sandia National Laboratories

ABSTRACT

This work explores the high-load limits of HCCI for naturally aspirated operation. This is done for three fuels with various autoignition reactivity: *iso*-octane, PRF80, and PRF60. The experiments were conducted in a single-cylinder HCCI research engine (0.98 liter displacement), mostly with a CR = 14 piston installed, but with some tests at CR = 18. Five load-limiting factors were identified: 1) NO_x-induced combustion-phasing run-away, 2) wall-heating-induced run-away, 3) EGR-induced oxygen deprivation, 4) wandering unsteady combustion, and 5) excessive exhaust NO_x.

These experiments at 1200 rpm show that the actual load-limiting factor is dependent on the autoignition reactivity of the fuel, the selected CA50, and in some cases, the tolerable level of NO_x emissions. For iso-octane, which has the highest resistance to autoignition of the fuels tested, the NO_x emissions become unacceptable at $IMEP_g$ = 473 kPa. This happens before wandering and unsteady combustion becomes an issue for $IMEP_g$ > 486 kPa. The NO_x is caused by high peak-combustion temperatures resulting from the high intake temperature required for this low-reactivity fuel. Iso-octane operation with a CR = 18 piston reduces the intake-temperature requirement. Consequently, the exhaust NO_x issue vanishes while the $IMEP_g$ can be increased to 520 kPa before wall-heating-induced run-away become an issue. For a very reactive fuel like PRF60, large amounts of EGR are required to control the combustion phasing. Therefore, the maximum $IMEP_g$ becomes limited at 643 kPa by the available oxygen as the EGR gases displace air. A fuel of intermediate reactivity, PRF80, exhibits the highest $IMEP_g$ for the conditions of this study – 651 kPa. For this fuel, the maximum $IMEP_g$ becomes limited by NO_x-induced run-away. This happens because even small amounts of NO_x recycled via residuals enhance the autoignition sufficiently to advance the ignition point. This leads to higher peak-combustion temperatures and more NO_x formation, thus making a very rapid run-away situation inevitable.

INTRODUCTION

The homogeneous charge compression ignition (HCCI) combustion process offers good fuel economy and very low nitrogen-oxide (NO_x) and particulate emissions. Therefore, engine manufacturers are considering HCCI combustion as one option to improve the efficiency of the spark-ignited gasoline engine, and also to reduce NO_x aftertreatment requirement for the latest generations of compression-ignited diesel engines. However, several technical difficulties need to be resolved before HCCI can be widely implemented in production engines. Among these, controlling the combustion phasing and increasing the power output while maintaining acceptable pressure-rise rates (PRR) continue to be major issues.

The autoignition quality of the fuel is an important parameter impacting the design of HCCI engines and the methods used to control the combustion phasing and the heat-release rate (HRR). HCCI operation has been demonstrated for a variety of fuels that have autoignition qualities spanning a wide range [1,2,3,4].

The autoignition quality can also influence the observed power output. For example, Ref. [5] demonstrates that PRF80 (a 80/20 volume mix of the primary reference fuels, iso-octane and n-heptane) can provide substantially higher indicated mean effective pressure ($IMEP_g$) than iso-octane when operated with a fuel/air-equivalence ratio (ϕ) of 0.40. This happens because PRF80 is more reactive and can be operated with a lower intake temperature (T_{in}) compared to iso-octane. A lower T_{in} leads to higher charge density and thus more inducted fuel when ϕ is kept constant. In addition, the data in Ref. [5] show that the cycle-to-cycle variations increase with combustion-phasing retard for both fuels, but also that the two-stage autoignition PRF80 has less cycle-to-cycle variation for a given amount of combustion-phasing retard. This is an important aspect that potentially can help to reach higher loads since extensive combustion-phasing retard is required in order

to keep the PRR below acceptable limits as the fueling is increased.

For a given displacement, the power output is proportional to both the brake mean effective pressure (BMEP) and the engine speed. However, to limit the parameter space, this study compares the performance of the different fuels at a fixed engine speed of 1200 rpm and naturally aspirated operation. Both the engine speed and the intake-boost pressure influence the observed autoignition reactivity and the amount of low-temperature heat release (LTHR) [6]. Because of this, the differences between the fuels may grow or diminish for operation with boost and at other engine speeds. Also, the choice of compression ratio (CR) influences the performance of the engine/fuel combination [7,8,9]. These aspects should be considered when comparing the data presented here with data acquired at other operating conditions in other engines.

SCOPE AND OBJECTIVES

The main objective of this study is to experimentally investigate how the choice of fuel influences the maximum obtainable $IMEP_g$ while maintaining steady operation with acceptable PRR and NO_x emissions. Furthermore, and equally important, the load-limiting factor(s) will be identified for each operation condition. The fuels considered are iso-octane, PRF80 and PRF60. The engine speed was 1200 rpm and the engine was operated with P_{in} = 100 kPa, simulating naturally aspirated conditions. CR = 14 was used for all three fuels. In addition, iso-octane was also evaluated at a higher CR of 18 for which high-load data have been previously published by the authors [10].

Following the description of the experimental setup, data acquisition and analysis, this paper covers six areas:

1. The three fuels are compared at the same degree of charge dilution to highlight combustion-process differences that arise from variations in the autoignition reactivity.

2. The importance of adjusting the combustion phasing (CA50) with load is demonstrated for PRF80.

3. The fundamentals responsible for the beneficial heat-release-smoothing effects of combustion-phasing retard are reviewed using multi-zone modeling.

4. With adjustments of CA50 to maintain a moderate PRR of 5 bar/°CA[1], the $IMEP_g$ is pushed to the limit for each fuel.

5. A detailed examination is made of each fuel separately, whereby the load-limiting factors are identified and the load limits are explored for operation also at PRR = 3 and 7 bar/°CA.

6. Based on the potential importance of NO_x feedback via residuals, the sensitivity of CA50 to NO_x addition is measured for each fuel. These results are presented in the Appendix.

EXPERIMENTAL SETUP

The engine used for this study is based on a Cummins B-series diesel engine, which is a typical medium-duty diesel engine with a displacement of 0.98 liters/cylinder. A schematic of the setup is shown in Fig. 1. The configuration of the engine and facility is nearly the same as for previous studies [*e.g.* 5,6,10-12], except for one substantial change: a new CR = 14 piston is used. As the schematic in Fig. 1 shows, this piston features a hemispherical bowl in the center. Compared to the shallower scallop of the piston used previously, this results in slightly higher surface-to-volume ratio at TDC. In addition, some squish flow can be expected. Because of this, slightly higher heat-transfer rates were anticipated. However, both motored and fired operation indicated a minimal effect. For example, the reduction of the thermal efficiency was measured to less than 0.2% (*i.e.* less than 0.5% increase of the fuel consumption). The reason for the change in piston geometry was to facilitate the concurrent testing of a variable-valve timing (VVT) system (not reported here). In case of an accidental valve impact onto the piston, the new piston design reduces the risk of bending of the valve stem as the valve is being pushed up against the hydraulic pressure. However, for all tests presented here, the traditional camshaft - push rod - rocker arm arrangement was used. The custom-design piston provides a small topland-ring crevice, amounting to only 2.1% of the top-dead-center (TDC) volume, including the volume behind the top piston ring.

For all operating conditions, except for the NO_x sensitivity measurements presented in the Appendix, the engine was fueled using a fully premixed fueling system featuring an electrically heated fuel vaporizer. The intake gases were metered with separate sonic nozzles for air, CO_2, and N_2. To supply H_2O to the intake charge, a metering pump was used to draw water from a bottle placed on a digital scale and feed it into the fuel vaporizer. An auxiliary air heater mounted close to the engine was used to precisely control the intake temperature (Fig. 1). Engine specifications are listed in Table 1. A detailed description of the engine modifications for HCCI operation can be found in Ref. [12].

Cylinder pressure measurements were made with a transducer (AVL QC33C) mounted in the cylinder head approximately 42 mm off center. The pressure transducer signals were digitized and recorded at ¼° crank angle (CA) increments for at least 100 consecutive cycles. (Except for the NO_x sensitivity data, for which 40 alternate-fire cycles were recorded.) The reported PRRs are computed based on the maximum pressure-rise rate averaged over at least 100 cycles (each cycle is analyzed separately with a linear fit over a moving

[1] At the conditions studied, the engine knock/ringing is not considered unacceptable until PRR > 8 bar/°CA.

TABLE 1. Engine Specifications

Displacement (single-cylinder)	0.981 liters
Bore	102 mm
Stroke	120 mm
Connecting Rod Length	192 mm
Nominal Geometric Compression Ratio	14:1
No. of Valves	4
IVO	0°CA*
IVC	202°CA*
EVO	482°CA*
EVC	8°CA*
Intake Air Swirl Ratio, Both Ports Combined	0.9

* 0°CA is taken to be TDC intake, so TDC combustion is 360°CA. The same camshaft is used as in previous studies, but the presented numbers for valve closing and opening are slightly adjusted to better represent the timing for 0.1 mm lift.

±0.5°CA window after low-pass filtering (< 2.5 kHz)). Similarly, the 50% burn point (CA50) was first computed from the low-pass filtered pressure trace for each individual cycle (without heat-transfer correction), and then averaged. However, it should be noted that for operation with the presence of LTHR, the LTHR is excluded when the cumulative heat release is computed. Effectively, the reported combustion phasings refer to CA50 for the main combustion event, starting at the crank angle of minimum heat-release rate between the low- and high- temperature combustion events. Presenting the data referring to the main combustion event alone is considered more relevant from the standpoint of quantifying the timing of the main combustion event.

Charge temperatures during the closed part of the cycle (*i.e.* compression/expansion) are computed using the ideal-gas law in combination with the measured pressure (ensemble-averaged over at least 100 cycles, except for Fig. 24b), the known cylinder volume, and the trapped mass. The average molecular weight used for the calculation during the compression stroke corresponds to that of the trapped gases - including fresh gases, EGR and retained residuals, and the fuel. During the combustion event, and in proportion to the mass fraction burned, the molecular weight gradually changes to that of the measured exhaust composition. This exhaust molecular weight is then used for the remainder of the expansion stroke.

The fuels used were blends of the primary reference fuels (PRF), iso-octane and n-heptane. The PRF blends allow selection of autoignition reactivity by varying the blending proportions. They are also fairly volatile, and this facilitates the charge preparation. Table 2 shows the fuel compositions and other relevant parameters.

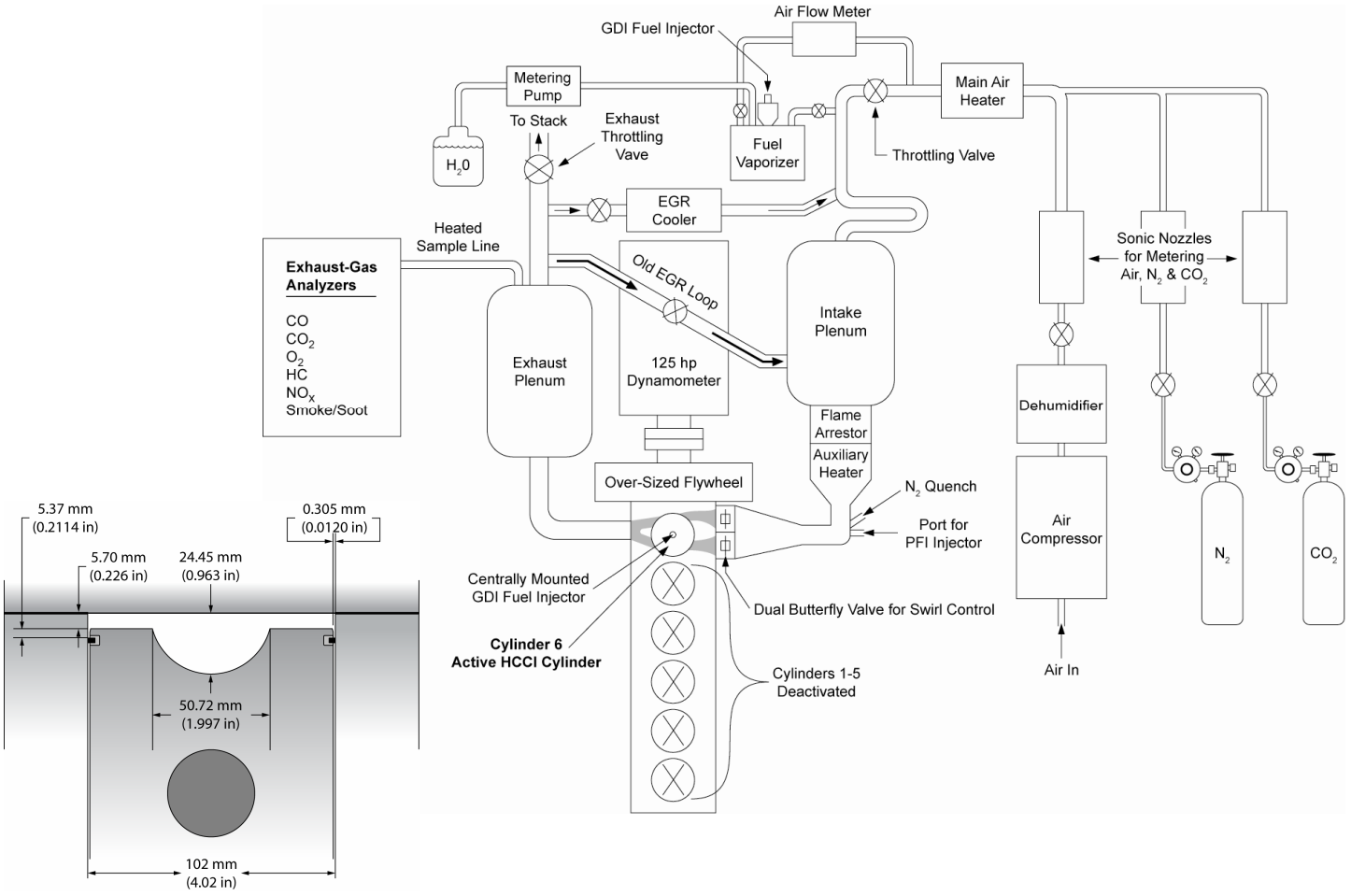

Figure 1. Schematic of the HCCI engine facility, and combustion-chamber dimensions at TDC with the CR = 14 piston.

TABLE 2. Fuel Properties

Fuel	Iso-Octane	PRF80	PRF60
Iso-Octane %vol.	100	80	60
n-Heptane %vol.	0	20	40
C-atoms	8	7.78	7.57
H-atoms	18	17.56	17.14
Molecular weight	114.23	111.15	108.21
A/F Stoichiometric	15.13	15.14	15.15
Lower heating value for gas-phase fuel [MJ/kg fuel]	44.65	44.71	44.76
Lower heating value for stoichiometric charge [MJ/kg air-fuel mixture]	2.769	2.770	2.772
Boiling point / range at 1 atm [°C]	99.2	98.4* - 99.2	98.4* - 99.2

* The boiling point for pure n-heptane is 98.4°C.

Because HCCI combustion is very sensitive to temperature, the engine coolant and oil were both fully preheated to 100°C before starting the experiments. In addition, the intake tanks and plumbing were preheated to at least 50°C to avoid any condensation of the water supplied with the simulated EGR. For all data presented, 0°CA is defined as TDC intake (so TDC compression is at 360°). This eliminates the need to use negative crank angles or combined bTDC, aTDC notation.

BASIC EGR CONSIDERATIONS

In an engine operating lean with complete combustion, EGR consists of air and complete stoichiometric products (CSP). Typically there are combustion inefficiencies, and this generates trace species like carbon monoxide (CO), hydrocarbons (HC) and partially-oxidized hydrocarbons. In addition, NO_x can be formed if the combustion temperatures are sufficiently high. All these species can potentially influence the autoignition. To avoid the influence of these combustion by-products, and to simplify the interpretation of the data, this study uses simulated EGR (except for Figs. 5 and 6, which use real EGR via the "old EGR loop" shown in Fig. 1). The simulated EGR consists of a mixture of air with the three components of complete stoichiometric products (CSP),

TABLE 3. Composition of simulated EGR (CSP) for all three fuels (% mole fraction). Average molecular weight (M) is also given.

Fuel:	Iso-Octane	PRF80	PRF60
CO_2	12.47	12.45	12.44
H_2O	14.03	14.05	14.08
N_2	73.50	73.49	73.48
M	28.71	28.71	28.70

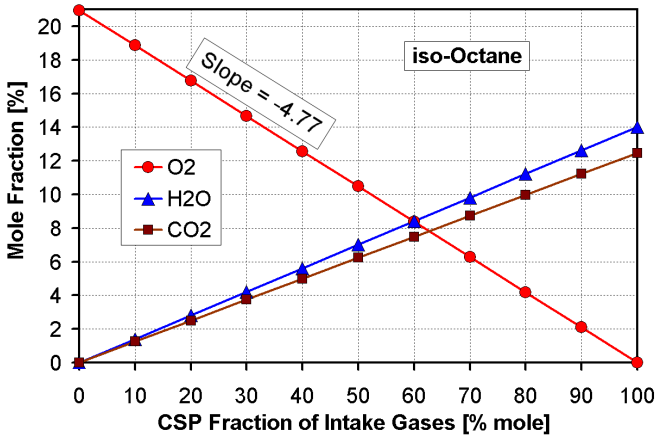

Figure 2. Intake mole fraction of O_2, CO_2, and H_2O as a function of CSP mole fraction. Excluding fuel.

namely CO_2, H_2O and N_2. The relative proportions of these components vary slightly with fuel-type and can be computed based on the average number of C and H atoms listed in Table 2. For iso-octane, complete stoichiometric combustion can be written as:

$$C_8H_{18} + 12.5\ (O_2 + 3.773\ N_2) \Rightarrow 8\ CO_2 + 9\ H_2O + 47.16\ N_2$$

where atmospheric argon and CO_2 have been lumped into the atmospheric N_2, following Ref. [13]. For complete combustion with ϕ = 1, the gas composition (excluding fuel) changes from: 20.95% O_2 and 79.05% N_2 for intake air, to products with 12.47% CO_2, 14.03% H_2O and 73.50% N_2 for wet exhaust. This exhaust composition will be referred to as CSP. As Table 3 shows, the CSP composition varies only marginally with changes in PRF number.

To simulate various amounts of EGR, air and CSP were metered into the intake system to form a homogeneous mixture. Figure 2 demonstrates how the intake gas composition changes with CSP mole fraction. The mole fractions of CO_2 and H_2O ($[CO_2]$ and $[H_2O]$) both increase linearly with increasing fraction of CSP, while $[O_2]$ decreases linearly. When evaluating data with simulated EGR, it can be beneficial to consider the intake $[O_2]$. For such cases, Fig. 2 can be used to convert the given %CSP to $[O_2]$.

RESULTS

INTAKE TEMPERATURE CONSIDERATIONS

This study compares the load capabilities of three fuels with different autoignition reactivities. As discussed in the introduction, the intake-temperature requirement can influence on the observed $IMEP_g$. Therefore, the intake temperatures that were used in this study are discussed first.

Plotted in Fig. 3b is the T_{in} that was used for each fuel type at a fueling rate corresponding to a charge[2]/fuel mass ratio (C/F) of 34.4 and a PRR of 5 bar/°CA. Iso-

[2] The charge mass is the sum of the supplied air and CSP constituents, excluding the fuel.

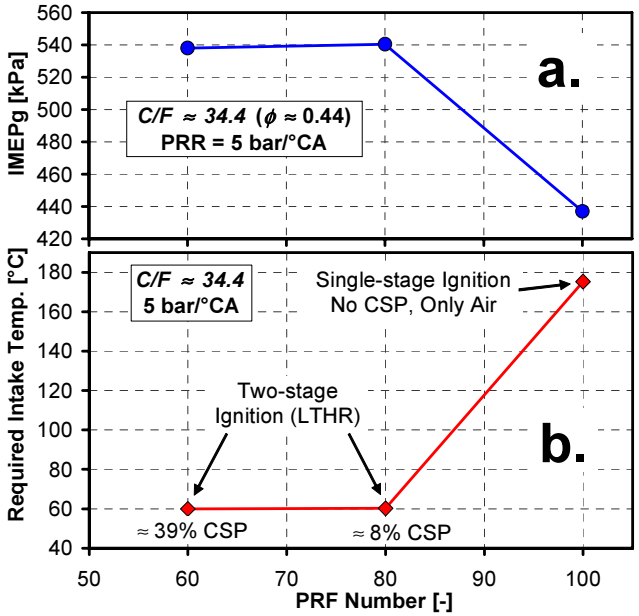

Figure 3. $IMEP_g$ and T_{in} as a function of PRF number for operation with air dilution only for iso-octane, and with CSP addition for PRF80 and PRF60. 1200 rpm. C/F ≈ 34.4, corresponding to ϕ = 0.44, had there been no CSP addition.

octane was operated with air dilution only (no CSP or real EGR), so the required T_{in} was determined by the CA50 that gives a PRR of 5 bar/°CA. As can be seen, iso-octane (PRF100) required a relatively high T_{in} of 175°C. This happens because iso-octane exhibits single-stage ignition at these operating conditions[3]. On the other hand, PRF80 and PRF60 exhibit two-stage ignition with LTHR for these operating conditions, as evident in Fig. 4c. This LTHR accelerates the temperature rise towards the end of the compression stroke and around TDC, shown in Fig. 4b. Therefore, T_{in} has to be reduced in order to achieve an appropriate combustion phasing after TDC. However, both PRF80 and particularly PRF60 are so reactive that without EGR it would have been necessary to drop T_{in} well below ambient for the higher fueling rates investigated. Clearly, this is not practical. Instead, T_{in} was set to 60°C to avoid condensation of water in the intake system and CA50 was then controlled by adjusting the amount of CSP.

As shown by the annotation in Fig. 3b, PRF80 required 8% CSP to achieve PRR = 5 bar/°CA, while PRF60 required 39%. Figures 4a and 4b show that this CSP addition makes both the temperature and pressure rise associated with LTHR comparable for the two PRF blends. Furthermore, Fig. 3a shows how the $IMEP_g$ varies between these fuels. PRF80 and PRF60 exhibit the highest power output and iso-octane the lowest. This happens because P_{in} was maintained at 100 kPa while

[3] As shown in Ref. [2], iso-octane can exhibit two-stage ignition with LTHR under conditions of elevated intake pressure. Also, low engine speed can allow the development of LTHR even for naturally aspirated conditions [14].

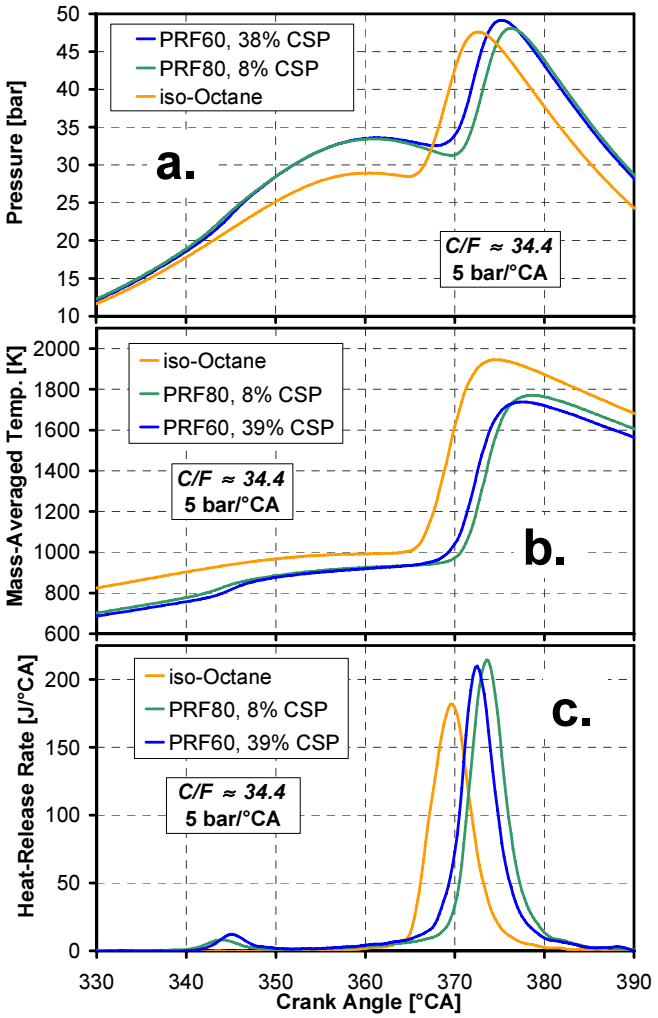

Figure 4. Pressure, temperature and HRR traces for operation with PRR = 5 bar/°CA and C/F ≈ 34.4.

C/F ≈ 34.4. Since a higher T_{in} lowers the charge density, less charge mass is inducted for each intake stroke for the iso-octane case. For this example with C/F ≈ 34.4 for all fuels, this also means that less fuel mass is inducted for the iso-octane case. This explains why iso-octane has 19% lower $IMEP_g$ in this example. As will be discussed below, higher $IMEP_g$ can be achieved with iso-octane by increasing the fueling rate. Nonetheless, it will be clear that the higher required T_{in} for iso-octane is detrimental for its high-load limits. On the other hand, the T_{in} requirement can be reduced by using a higher CR, and this will also be examined.

ADJUSTMENTS OF CA50 FOR CONSTANT PRR

For HCCI to be practical for automotive use, fairly wide load ranges must be covered. Within the load range, the combustion phasing must be easy to control in a robust and repeatable manner. As will be clear from the results presented below, the combustion phasing generally becomes more sensitive to small disturbances in charge temperature and composition as the load is increased towards the upper load limit. This work does not consider operation with closed-loop CA50 control which

can allow continuous operation at combinations of CA50 and fueling rate that spontaneously lead to misfire or uncontrollable combustion-phasing advancement (*i.e.* run-away) [7]. Instead, the upper load limit in this study is determined by the combination of fueling and CA50 which can be operated continuously and steadily by only applying slow (~minute timescale) adjustments of T_{in} (for iso-octane) and CSP/EGR rate (for PRF80 & PRF60) to correct for minor disturbances. As will be shown, above this $IMEP_g$ limit it becomes impossible to obtain steady operation. However, the factor that makes steady operation impossible often changes with both fuel type and CA50, as will be shown.

In the process of determining these steady-state high-load limits, the fueling rate was increased stepwise from moderate fueling rates to high fueling rates while data were recorded for each steady operating point. To allow efficient data acquisition and subsequent comparison between fuels, as many parameters as possible should be held constant as the fueling rate is increased. In previous studies by the authors, data were often compared at a fixed CA50 [*e.g.* 6,11,12]. However, when spanning very wide ranges of fueling rates up to the load limit, it becomes impossible to work with a predetermined CA50 while maintaining acceptable engine performance.

This point is illustrated by the two cases shown in Figs. 5 and 6. First consider the case where CA50 is held fixed, as shown by the red diamonds in Fig. 5. Figure 5a shows how the PRR changes with fueling rate ($IMEP_g$) when CA50 is held fixed at 372°CA by adjusting the EGR rate for each operating point. The corresponding pressure traces are shown in Fig. 6a. As can be seen, the PRR increases rapidly with increasing fueling rate. This happens because the total pressure rise is higher (Fig. 6a) while the combustion duration decreases (Fig. 5c). For $IMEP_g$ > 560 kPa, the PRR exceeds the acceptable level of 8 bar/°CA, which corresponds to a ringing intensity of 5 MW/m^2 [10,11,14,15]. Conversely, if the fueling rate is reduced significantly below the plotted range, the combustion becomes so slow that combustion inefficiencies arise, along with increasing risk for complete misfire.

These problems can be avoided if CA50 is adjusted with fueling rate such that a reasonable PRR is maintained across the $IMEP_g$ range of interest. This is demonstrated by the curves with blue squares in Fig. 5. The corresponding pressure traces are shown in Fig. 6b. Figure 5b shows how CA50 has to be adjusted with fueling rate to maintain a constant PRR of 7 bar/°CA (Fig. 5a). As can be seen, a more retarded CA50 is required when the fueling is increased. In addition to avoiding excessive ringing, Fig. 6b shows that the more retarded CA50 for higher fueling rates leads to a slight reduction of the peak combustion pressures, despite the higher $IMEP_g$. In contrast, the constant-CA50 data show a substantial increase of the peak pressure for increased fueling rates (Fig. 6a). Finally, with a constant PRR, the combustion duration is also constant, as shown in

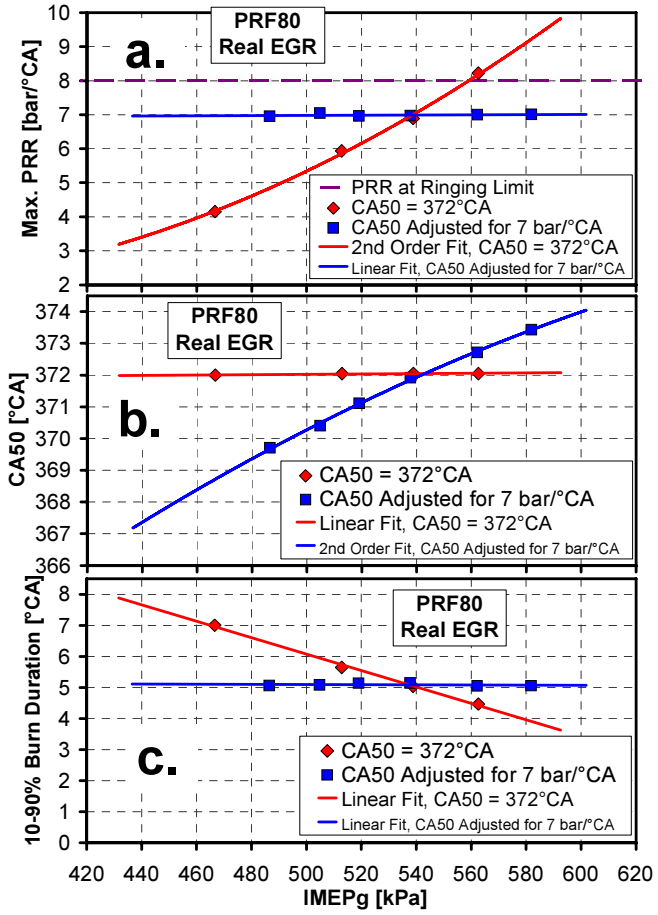

Figure 5. a) PRR as a function of $IMEP_g$ both for operation with CA50 = 372°CA and with CA50 variable, b) corresponding CA50, c) corresponding 10-90% burn duration.

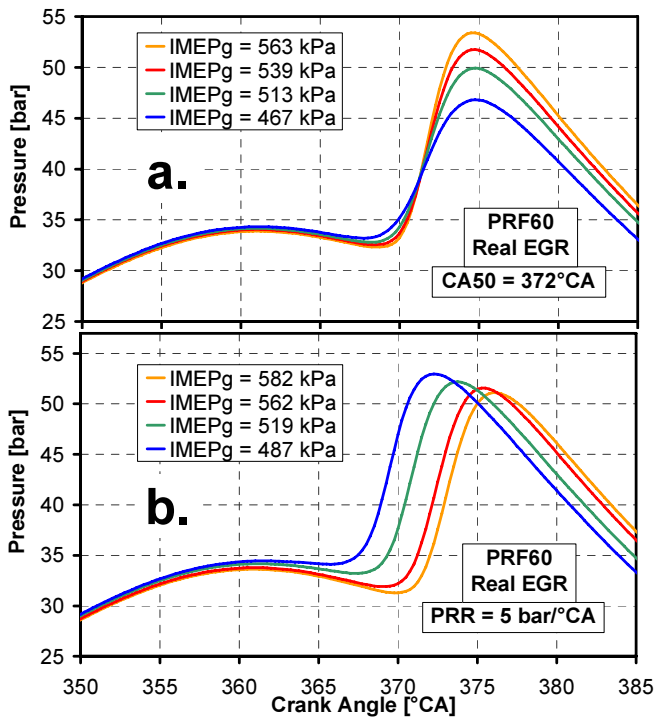

Figure 6. Pressure traces corresponding to Fig. 6. a) CA50 = 372°CA. b) CA50 variable to obtain PRR = 5 bar/°CA.

Fig. 5c. The fundamentals behind these important benefits of CA50 retard will be reviewed in the following section.

It is important to maintain high thermal efficiency of the HCCI engine. Retarding CA50 reduces the effective expansion ratio and can potentially reduce the thermal efficiency. However, because the piston motion is small around TDC, it is not until CA50 > 372°CA that a substantial impact on the thermal efficiency is noted. Even so, it is not a viable option to limit the CA50 retard to 372°CA since operation with excessive PRR leads to increased wall heat transfer and even larger reductions of the thermal efficiency than does CA50 retard. Further discussion of this is given in the Summary and Conclusions.

RELATIONSHIP BETWEEN CA50, FUELING RATE AND PRR

As discussed above, and shown in Fig. 6b, an acceptable PRR can be maintained by retarding CA50 as the fueling is increased. Since this beneficial effect of combustion-phasing retard is necessary for high-load HCCI operation, it is helpful to review the fundamental principles behind this effect. Figure 7 shows computational results, some of which were originally presented in Ref. [16]. The chemical-kinetics model has five adiabatic temperature zones which are coupled through the in-cylinder pressure. (A complete model description can be found in Ref. [16].) Three cases with different CA50 are presented in Fig. 7b. The corresponding sets of 5-zone temperature traces are given in Figs. 7c-e, respectively. These computations show that retarded combustion phasing leads to a strong reduction of the PRR when ϕ is maintained constant at 0.45 (Fig. 7b). This does not happen because the local high-temperature combustion reactions become slower [14]. In fact, Figs. 7c-e show that the temperature rise is nearly vertical for each burning zone, regardless of the combustion phasing. Based on this observation, it can be concluded that the overall combustion duration is determined almost entirely by the autoignition dwell between subsequently colder zones, not the local high-temperature reaction rate. In combination with the longer dwell between zones, the greater piston expansion leads to lower PRR for the more retarded cases shown in Fig. 7b.

The autoignition dwell between subsequently colder zones is principally determined by the actual thermal distribution, or thermal width (TW) of the charge [14,16]. However, to explain the much larger dwell between temperature zones in Fig. 7e compared to Fig. 7c, we have to consider the coupling between the in-cylinder pressure and the compression heating of subsequently colder zones. The hottest zone for each of the cases in Fig. 7 can be thought of as representing the close-to-adiabatic core in the experiment. This hottest zone will autoignite according to the charge temperature at BDC (in combination with the given CR). Within the range of ϕ encountered for moderate to high loads in HCCI engines, the combustion is fast and complete, so a

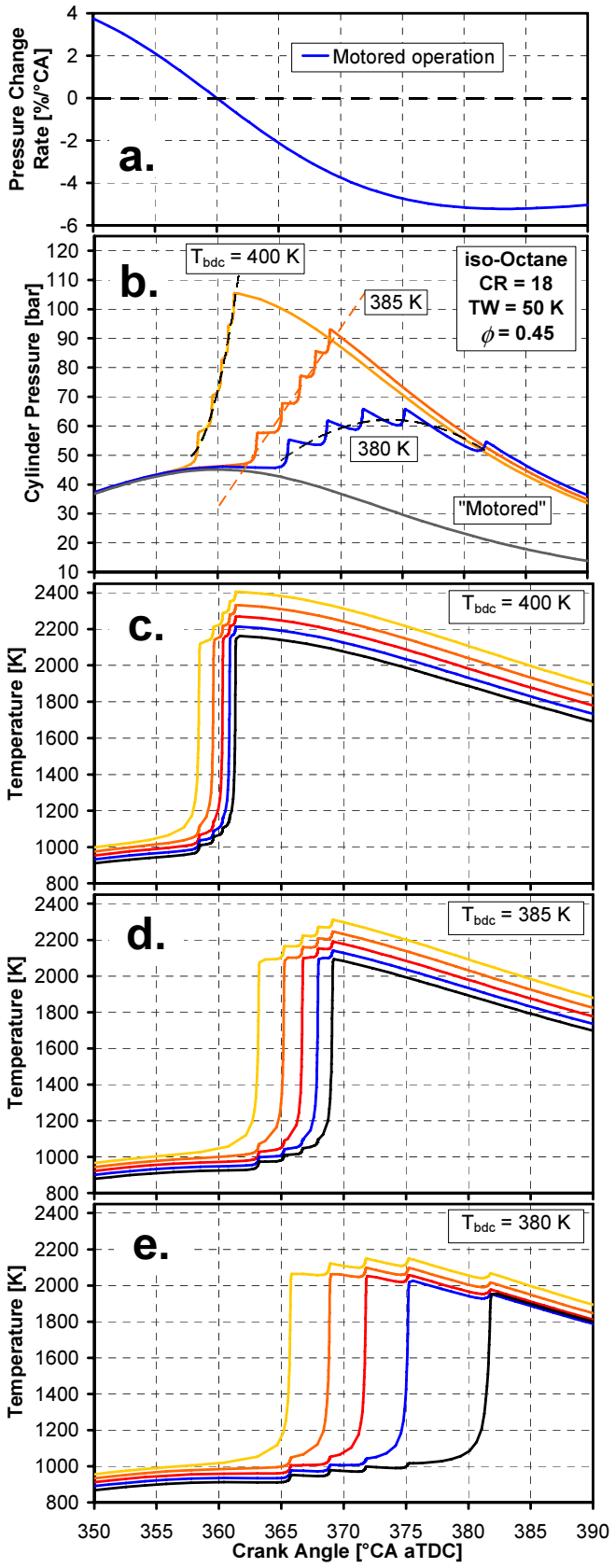

Figure 7. a.) Pressure-change rate as a function of crank angle for "motored" operation. b.) Effect of combustion phasing on PRR. $T_{bdc,max}$ for each case is indicated in the graph. c-e.) Temperature traces for each zone in the three 5-zone cases shown in b. Iso-octane, ϕ = 0.45, 20% mass per zone. Expanded from Fig. 13a in Ref. [16].

distinct amount of pressure rise can be associated with the combustion of the hottest zone due to the increase of its gas temperature.

This pressure rise due to combustion of the first zone leads to a compression of the not-yet-ignited zones. However, the amount of compression, and therefore the amount of compression heating, is influenced by the concurrent piston motion. As Figs. 7a and 7b show, the piston motion after TDC leads to an increasing rate of pressure drop. This subtracts from the pressure rise associated with combustion of any temperature zone, thus leading to less compression heating and longer autoignition dwell between subsequently colder zones. This is the main reason why the PRR is reduced with CA50 retard.

It is also important to consider the effect of the actual piston position on the magnitude of the pressure rise associated with combustion of a given thermal zone. When the heat release occurs later and the combustion-chamber volume is larger, there will be less pressure rise. This happens because the increase of the average charge temperature per unit of released heat is nearly invariant of the combustion-chamber volume. Applying the ideal gas law, it follows that there will be a direct reduction of the pressure rise per unit of released heat when the volume is larger, since the gas has a lower density. This contributes to a lower PRR since the total pressure rise during the whole combustion event is reduced. In addition, there will be an indirect reduction of the PRR since the smaller pressure rise also reduces the compression heating of the not-yet-ignited zones. Therefore, the larger combustion-chamber volume will contribute to increased dwell between subsequently colder zones, similarly to the discussion with respect to the piston-expansion rate in the previous paragraph.

Another contribution to the experimentally observed reduction of PRR with CA50 retard is not captured by this adiabatic model. CFD modeling performed in Ref. [10] shows that the thermal width of the charge increases somewhat during the early expansion stroke due to the effects of wall heat transfer and mixing. This effect contributes to some extent to a longer combustion duration for more retarded combustion phasing.

For better understanding of the results shown in Figs. 5 and 6, it is helpful to recognize that the amount of pressure rise associated with the combustion of the hottest zone is nearly directly proportional to the fueling rate. Therefore, an increased fueling rate leads to more compression-heating of not-yet-ignited zones. Consequently, for a given CA50, a higher fueling rate will result in less ignition delay between subsequently colder zones. This results in a shortening of the overall burn duration, as shown experimentally in Fig. 5c. The shorter burn duration in combination with the larger total pressure rise for more fuel burned makes the PRR increase quickly, as Fig. 5a shows. To compensate for the more forceful combustion-driven compression of the colder zones at higher fueling rates, CA50 can be further retarded so that both the piston-expansion rate and the combustion-chamber volume during the combustion event become greater. When CA50 is adjusted according to Fig. 5b, both the combustion duration (Fig. 5c) and the PRR can be maintained constant (Fig. 5a).

These beneficial effects of combustion-phasing retard have also been examined experimentally in previous works [5,10,16]. However, combustion-phasing retard must be applied carefully since excessive retard can lead to partial-burn events, or complete loss of combustion [5,10].

HIGH-LOAD LIMITS FOR ALL FUELS AT 5 BAR/°CA

The above discussion in conjunction with Figs. 5 and 6 demonstrates the beneficial effects of adjusting CA50 with fueling rate. For the purpose of minimizing the number of changing parameters, all subsequent measurements were conducted for fueling sweeps with a constant pre-selected PRR. However, as will be discussed below, the optimal PRR may change with fueling rate and design objectives. As a starting point, a moderate PRR of 5 bar/°CA is used below when exploring the high-load limits at these conditions (naturally aspirated operation at 1200 rpm). This is followed by a more detailed treatment of each fuel in the following sections.

Figure 8 shows data plotted against the fueling rate in mg/cycle. As can be seen, the fueling ranges are different for each fuel. The highest fueling rate for each fuel was determined by the upper load limit, which is the main interest of this study. However, to better understand the reason for the upper load limit, it is beneficial to perform measurements over a range of fueling rates. For iso-octane, the lowest fueling rate was selected arbitrarily and corresponds to ϕ = 0.382. The NO_x emissions are near-zero for this ϕ (Fig. 11 – to be discussed below). For PRF80 and PRF60, the lowest fueling rate was determined by the preset T_{in} = 60°C. Operating without CSP addition, this T_{in} determines what fueling rate will result in a PRR of 5 bar/°CA. Because PRF60 is much more reactive than PRF80, it can also be operated at a lower fueling rate when the only dilution is air. On the other hand, PRF60 requires much more CSP addition at the highest loads, as Fig. 8a shows.

Figure 8b plots the $IMEP_g$ obtained as a function of fueling rate. The highest $IMEP_g$ point for each fuel is represented by the larger black symbols. As can be seen, iso-octane can obtain an $IMEP_g$ up to 481 kPa. The two-stage ignition fuels can produce significantly higher $IMEP_g$. PRF80 produces up to 651 kPa, while PRF60 produces up to 638 kPa. Within each respective $IMEP_g$ range, all fuels operate with low cycle-to-cycle variation of the $IMEP_g$, as plotted against the right-hand axis in Fig. 8b. The main reason why the two-stage ignition fuels can produce 33-35% higher $IMEP_g$ is the lower T_{in}. As pointed out above, PRF80 and PRF60 were operated with T_{in} = 60°C, while iso-octane required T_{in} =

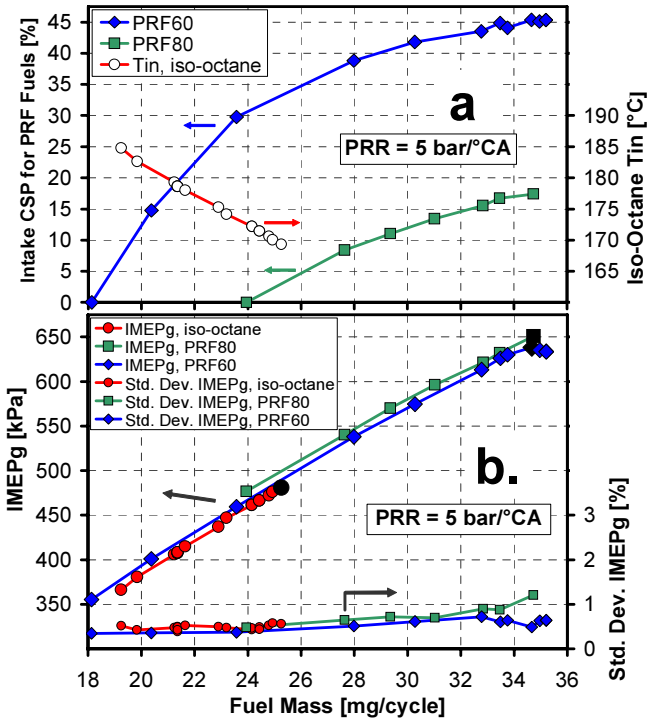

Figure 8. a) Fraction CSP in the intake (T_{in} for iso-octane) required to maintain PRR = 5 bar/°CA as a function of fueling rate. b) $IMEP_g$ and standard deviation of $IMEP_g$. The larger black symbols represent the highest steady-state $IMEP_g$ for each fuel type.

169°C at the highest load (Fig. 8a). This allows PRF80 and PRF60 to induct 21-22% more gas mass per cycle. In addition, PRF80 and PRF60 can be operated with lower C/F – in other words, they allow more fuel per unit charge mass. The C/F for the highest $IMEP_g$ points are 30.7, 27.1 and 26.7 for iso-octane, PRF80 and PRF60, respectively. For reference, had there been no CSP addition, which lowers the intake [O_2], these C/F ratios would correspond to ϕ = 0.493, 0.559 and 0.567, respectively.

Figure 9 shows how CA50 had to be adjusted with $IMEP_g$ in order to maintain PRR = 5 bar/°CA. The iso-octane and PRF80 data coincidentally fall on the same line. For these two fuels, CA50 has to be retarded on the order of 2°CA for every 50 kPa increase of the $IMEP_g$. In the higher $IMEP_g$ range, PRF60 allows CA50 to be slightly (~1.5°CA) more advanced compared to PRF80. This could be related to the higher CSP fraction (Fig. 8a) for PRF60, which slows down the combustion. In the lowest $IMEP_g$ range, PRF60 allows almost 6°CA more advanced CA50. This is likely related to the slow combustion for PRF60 due to the lean conditions. ϕ = 0.285 for the lowest PRF60 point, while it is ϕ = 0.382 for the lowest iso-octane point. With ϕ = 0.285, the chemical-kinetics are sufficiently slow to make the burn duration longer compared to a higher-ϕ case, for which the burn duration is primarily determined by the thermal in-cylinder distribution, as discussed in conjunction with Fig. 7. In the following, the factors that ultimately prevent higher $IMEP_g$ will be identified for each fuel.

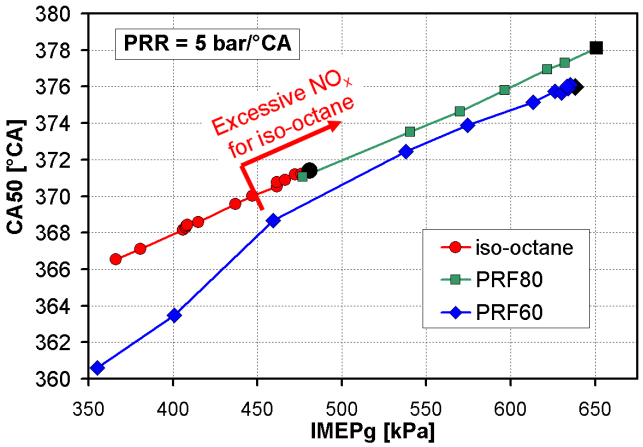

Figure 9. CA50 as a function of $IMEP_g$ for each fuel type.

LOAD-LIMITING FACTORS FOR ISO-OCTANE

PRR = 5 bar/°CA - At a PRR of 5 bar/°CA, iso-octane can obtain an $IMEP_g$ up to 481 kPa, as discussed above in conjunction with Fig. 8. However, as the annotation in Fig. 9 suggests, before this upper $IMEP_g$ has been reached, the NO_x emissions become unacceptable. So in this sense, iso-octane has two high-load limits. The excessive NO_x emissions are discussed first.

Figure 10 shows pressure and temperature traces for selected fueling rates. Despite the more retarded CA50 for the higher $IMEP_g$, the peak combustion temperature increases significantly within the examined load range. This is also clear from the left-hand axis in Fig. 11, which plots the peak mass-averaged charge temperature as a function of ϕ. Within this range of peak combustion temperatures, the NO_x emission increases quickly with increased ϕ, as the data plotted against the right-hand axis in Fig. 11 show. Depending on the actual emissions legislation, NO_x can be the load-limiting factor. In Fig. 11 the US2010 heavy-duty specific NO_x emissions limit of 0.27 g/kWh is represented by the horizontal dashed line. With regards to this limit, the NO_x emissions become unacceptable for ϕ > 0.457. As Fig. 9 shows, this creates an $IMEP_g$ limit of 448 kPa.

For situations with less stringent engine-out NO_x emissions requirements, it may be of interest to operate with $IMEP_g$ > 448 kPa. For such cases, the upper $IMEP_g$ which can be operated steady-state with PRR = 5 bar/°CA is 481 kPa, as discussed above. If the fueling is increased further, a steady-state operating condition cannot be established. Figure 12 illustrates the loss of combustion control that occurs for an $IMEP_g$ of 485 kPa at this operation condition with iso-octane. At first, the CA50 is fairly steady. However, beyond about 140 s it starts to advance at an increasing rate. Due to the advancement of CA50, the PRR increases greatly and at the end of the 2000-cycle sample it well exceeds the acceptable PRR limit of 8 bar/°CA. The correlation between higher PRR and more advanced CA50 is clear from a comparison of the curve fits in the 140 – 200 s

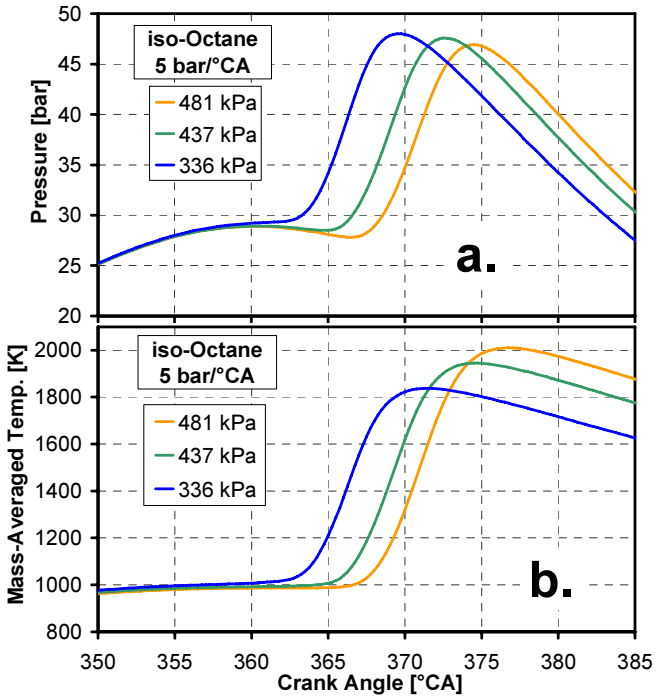

Figure 10. Pressure and temperature traces for selected $IMEP_g$ of 481, 437 and 336 kPa, corresponding to ϕ = 0.493, 0.450 and 0.382, respectively.

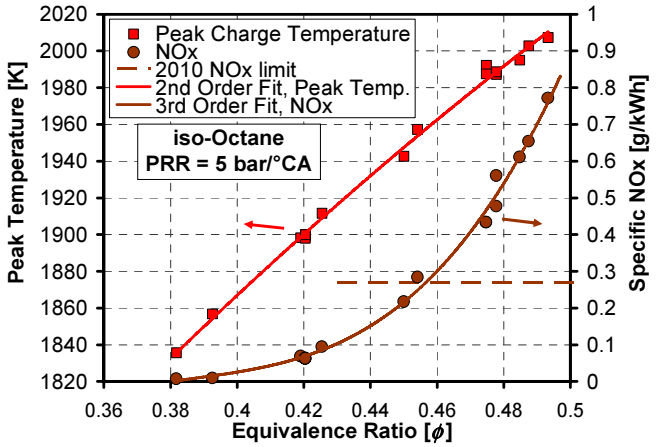

Figure 11. Peak mass-averaged temperature and specific exhaust NO_x emissions as a function of ϕ. The US2010 NO_x limit of 0.27 g/kWh is included for reference.

period. In the following, the causes of this run-away situation are examined.

In earlier work with the same engine, but with a CR = 18 piston, it was concluded that wall-heating-induced run-away caused the upper load limit [10]. This can happen since the heat-transfer losses, and therefore the wall heating, increase with increasing PRR and in-cylinder ringing [10,17]. Examination of Fig. 12 shows that during the run-away phase, CA50 advances approximately 1.5°CA for each 20 s period. To achieve the same rate of CA50 advance for a non-run-away situation, the firedeck temperature would have to be increased by

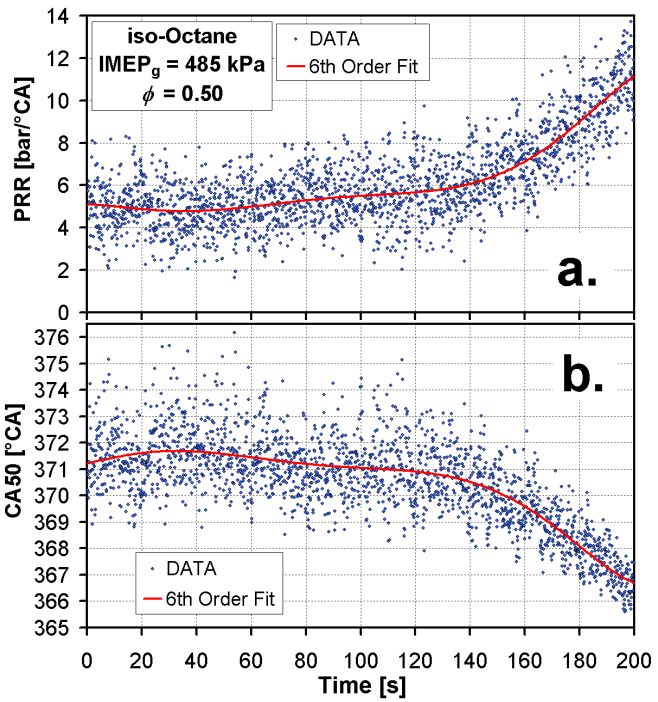

Figure 12. Example of wall-heating-induced run-away for iso-octane operation at a nominal PRR of 5 bar/°CA and $IMEP_g$ = 485 kPa.

roughly 5°C for each 20 s period[4]. This estimate coincides roughly with the observed increase of the wall temperature during run-away transients for iso-octane. As such, it strengthens the hypothesis that wall heating, which leads to progressively higher charge temperature for the subsequent cycles, is the cause for the observed run-away. Olsson *et al.* [7] were the first to describe this kind of run-away problem. They put forth a mathematical expression that defines how the sensitivities of wall temperature to combustion phasing and combustion phasing to wall temperature must relate to each other for steady operation. In the examples given in Ref. [7], CA50 advanced roughly 3°CA for each 20 s period. This is roughly twice as fast as the rate in Fig. 12. On the other hand, their engine was mostly operated boosted, and this could increase the wall heating, making the run-away occur faster.

If this run-away at the high-load limit indeed is caused by the coupling between CA50, PRR and wall heating, this coupling should also influence the sensitivity of CA50 to changes of T_{in} ($-dCA50/dT_{in}$) for normal operation without run-away. In fact, regression analysis of the plotted T_{in} data together with the corresponding CA50 data (not plotted) shows that the CA50 sensitivity to changes of T_{in} increases sharply at the high-load limit, as plotted against the right-hand axis in Fig. 13. Overall, the data at hand strongly indicate that wall-heating-induced run-away indeed causes the observed load limit for operation with iso-octane at PRR = 5 bar/°CA.

[4] Estimated from measured CA50 sensitivity to changes of the BDC temperature in combination with data showing the relationship between the coolant temperature and the BDC temperature, as acquired for Ref. [10].

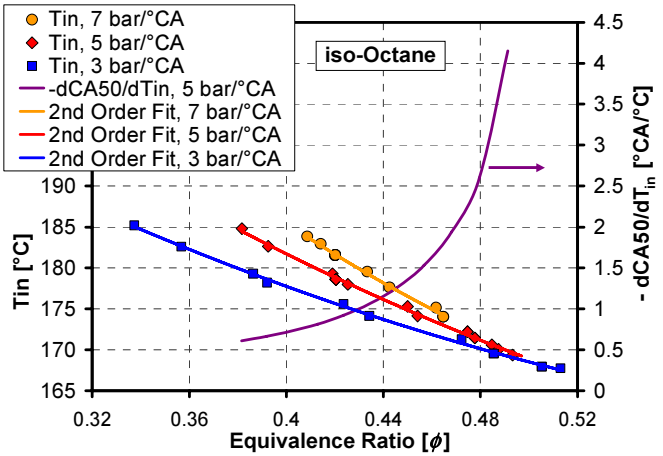

Figure 13. T_{in} required to maintain PRR = 3, 5, or 7 bar/°CA as a function of ϕ. Also plotted is the sensitivity of CA50 to changes of T_{in} ($-dCA50/dT_{in}$) for operation with PRR = 5 bar/°CA. This sensitivity is obtained by regression analysis of the plotted T_{in} data together with the corresponding CA50 data (not shown).

Load limits at other PRRs for iso-octane – Since the choice of CA50 influences both wall heating and peak combustion temperatures, it could be anticipated that the load limits may change if the engine is operated at a different PRR. Indeed, Fig. 14 shows that this is the case. Compared to the 5 bar/°CA data set, the 7 bar/°CA data set has a more advanced CA50. As expected, this leads to higher peak combustion temperature (not shown). Consequently, the onset of unacceptable NO_x emissions occurs at a lower $IMEP_g$ of 410 kPa, as indicated by the brown triangles in Fig. 14. Conversely, operating at a lower PRR with a more retarded CA50 allows higher $IMEP_g$ before NO_x emissions become unacceptable. Furthermore, the green squares in Fig. 14 show how the $IMEP_g$ at the control limit changes with PRR. For operation at 7 bar/°CA, run-away occurs already for $IMEP_g$ > 451 kPa. This happens because the wall heating is greater for operation with a higher PRR at a more advanced CA50.

On the other hand, operation with a more retarded CA50 and a lower PRR of 3 bar/°CA reduces wall heating and the risk for run-away is diminished. In fact, the control limit changes its character and becomes less well defined. Unlike operation at higher PRR, fast run-away was not observed at 3 bar/°CA. Instead, the cycle-to-cycle variations of CA50 become unacceptably high and the average combustion phasing also tends to wander back and forth. This is indicated by the annotation in Fig. 14. A typical history of CA50 is also plotted in Fig. 15. This wandering unsteady combustion is similar in nature to the run-away cases in the sense that it is not truly steady-state operation. However, the unsteadiness for such retarded operation is mostly caused by the high sensitivity of the autoignition timing to random temperature fluctuation, rather than large changes of the wall temperature with CA50. Because of this, rapid run-away does not happen as long as the engine operator continuously tweaks the intake temperature to limit the drift in CA50.

The fact that the CA50 starts to wander for high $IMEP_g$ when operated at a low PRR suggests that there is a trade-off between PRR, CA50, and the observed cycle-to-cycle variations. Indeed, Fig. 16 shows that for a

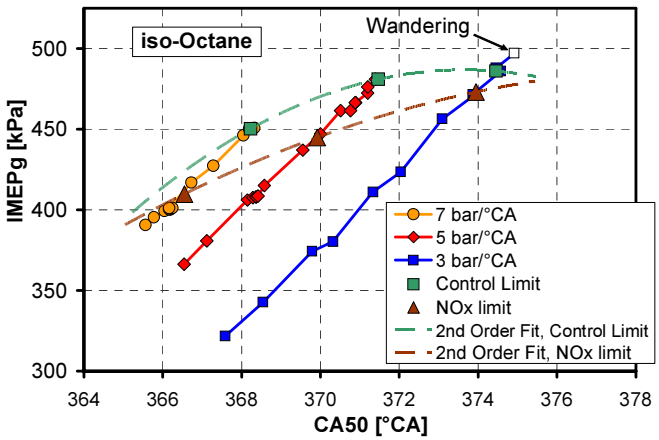

Figure 14. $IMEP_g$ plotted against CA50 for operation at PRR = 3, 5 & 7 bar/°CA. US2010 NO_x limit and control limit are also included.

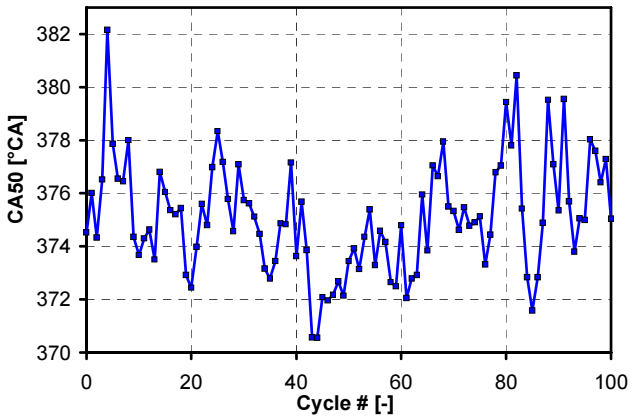

Figure 15. Wandering unsteady combustion with (on average) $IMEP_g$ = 497 kPa and PRR = 3 bar/°CA.

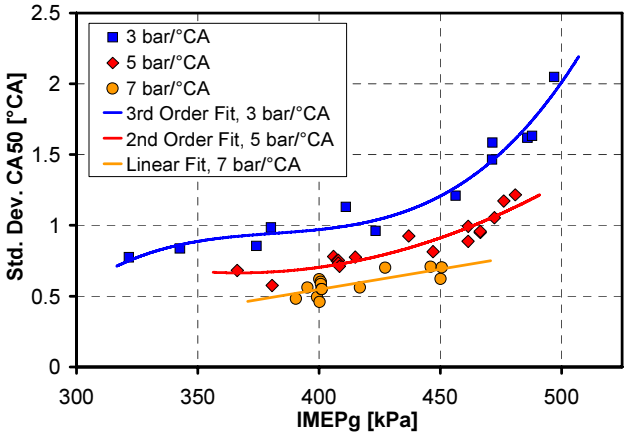

Figure 16. Standard deviation of CA50 as a function of $IMEP_g$ for operation with PRR = 3, 5 & 7 bar/°CA.

given $IMEP_g$, operation at a lower PRR results in higher standard deviation of CA50. Particularly, the CA50 variations increase rapidly for the highest $IMEP_g$ data points for the PRR = 3 bar/°CA data set. Thus, cycle-to-cycle combustion stability has to be factored in when designing an HCCI combustion system that includes highly retarded operation. For the conditions of this study, $IMEP_g$ = 486 kPa is considered the upper acceptable $IMEP_g$ limit for PRR = 3 bar/°CA. This $IMEP_g$ value is marked with a green square in Fig. 14. As Fig. 16 shows, the standard deviation of CA50 is 1.6°CA at this load limit.

ISO-OCTANE OPERATION WITH CR = 18

As pointed out in conjunction with Fig. 3b, the high T_{in} requirement for iso-octane reduces the inducted gas mass and therefore has a negative impact on the maximum $IMEP_g$. To investigate the potential benefit from operation at a higher CR, existing data with a CR = 18 piston [10] were reanalyzed. Figure 17 shows a comparison for operation with PRR = 5 bar/°CA. As can be seen in Fig. 17a, the highest obtainable $IMEP_g$ increases substantially from 481 to 520 kPa. Another benefit from the use of a higher CR is the mitigation of the NO_x emissions as a result of lower peak combustion temperatures. This happens because the same $IMEP_g$ is produced at a lower ϕ due to the lower required T_{in} (Fig. 17b), which increases the amount of inducted gas per cycle. The higher thermal efficiency at the higher CR

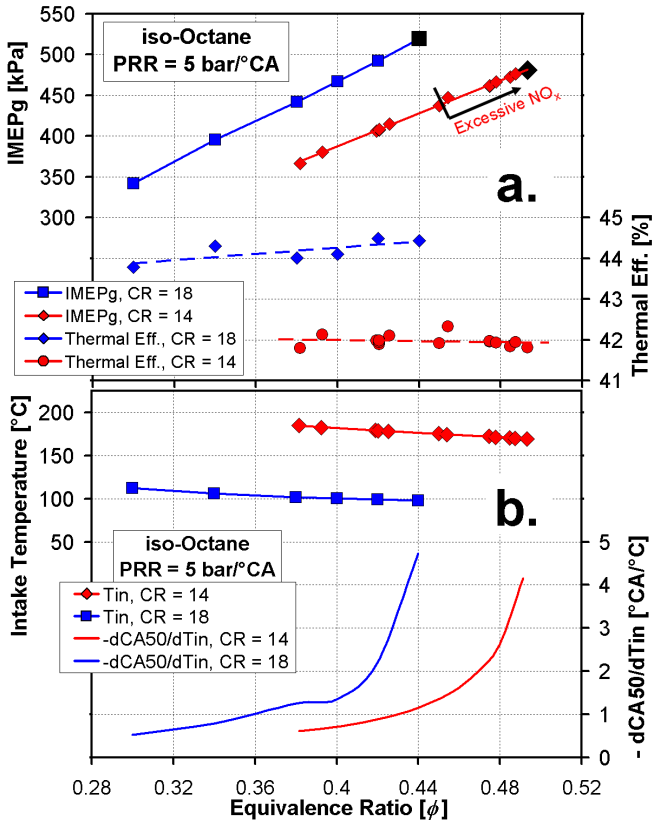

Figure 17. Comparison of operation with CR = 14 & 18 a) $IMEP_g$ and thermal efficiency as a function of ϕ. b) T_{in} and CA50's sensitivity to changes of T_{in} as a function of ϕ.

(Fig. 17a) also contributes to a lower ϕ for a given $IMEP_g$. Like operation with CR = 14, wall-heating-induced run-away occurs if the $IMEP_g$ is increased beyond 520 kPa. It is noteworthy that this run-away occurs at a significantly lower ϕ for CR = 18. As Fig. 17b shows, the thermal sensitivity of CA50 increases steeply at a lower ϕ for the CR = 18 case. As discussed above and in Ref. [10], this high thermal sensitivity is caused by the coupling between CA50 and wall heating, and the resulting influence of wall temperature on the temperature of the inducted gases.

Finally, it can be noted that a similar increase of the maximum $IMEP_g$ with higher CR has been observed also with the use of gasoline [9]. For these naturally aspirated operating conditions, gasoline exhibits single-stage ignition and requires high T_{in}, similar to iso-octane [18,19].

LOAD-LIMITING FACTOR FOR PRF80

Figure 9 shows that for PRF80, the highest $IMEP_g$ with steady engine operation is 651 kPa for PRR = 5 bar/°CA. When the $IMEP_g$ is increased further, rapid run-away occurs, as shown in Fig. 18. It is striking how much faster the run-away occurs for PRF80 compared to iso-octane. Note that the plotted time scale is expanded by a factor of four compared to that of iso-octane in Fig. 12 It takes only 10 s for the PRR to rise from 5 to 20 bar/°CA. This can be compared with the approximately minute-long run-away for iso-octane. The explanation for the faster run-away will be sought below. The $IMEP_g$ and fueling rate are both higher, so higher wall heat transfer is possible. On the other hand, for two-stage-ignition PRF80, CA50 is less sensitive to increasing charge temperature compared to single-stage-ignition iso-octane [5]. Because of these circumstances, it seems unlikely that wall heating is responsible for the rapid run-away shown in Fig. 18. Perhaps a chemical effect is causing the rapid run-away.

Figure 19 shows how the peak combustion temperature increases with increasing $IMEP_g$. As can be seen, a temperature of 1950 K is reached at the highest steady $IMEP_g$. This temperature corresponds well to the temperature above which NO_x became unacceptable for iso-octane, as plotted in Fig. 11. Indeed, the NO_x emissions are starting to rise for the highest $IMEP_g$ point for PRF80, as plotted against the right-hand axis in Fig. 19. Given how fast the NO_x emissions increase above 1950 K for iso-octane, and also how rapidly NO_x increases in Fig. 19, it can be expected that high levels of NO_x will be produced if the $IMEP_g$ is increased above 651 kPa for PRF80. Based on this, it is worthwhile to further examine the role of NO_x for the high-load limit. However, the performance for operation at other PRRs will be examined first.

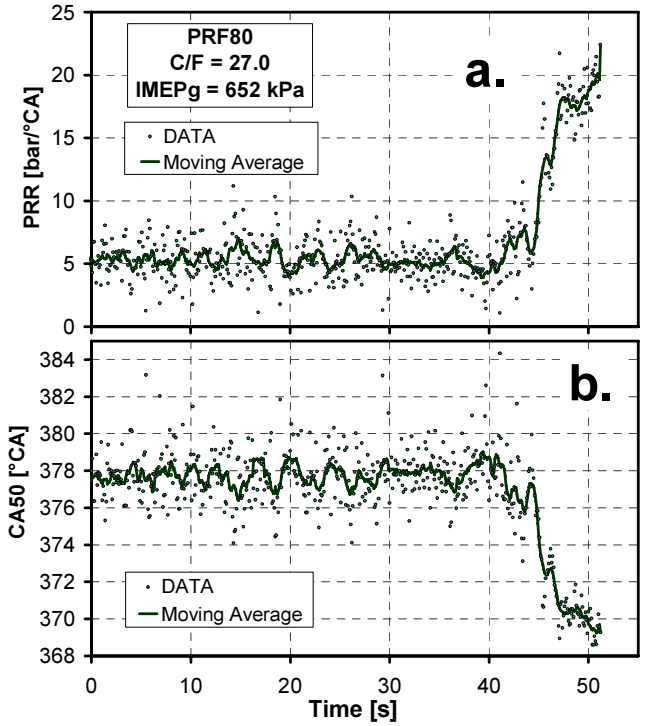

Figure 18. Rapid run-away for PRF80 when operated with $IMEP_g$ beyond the control limit at PRR = 5 bar/°CA

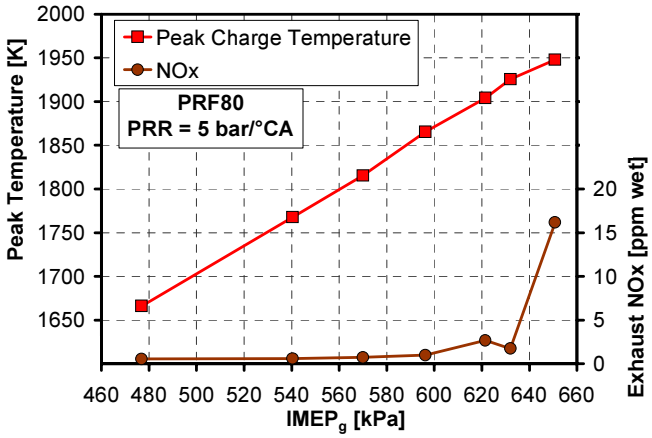

Figure 19. Peak charge temperature and exhaust NO_x emissions as a function of $IMEP_g$ for operation with PRF80 at PRR = 5 bar/°CA.

Load limits at other PRRs for PRF80 – Figure 20 shows how CA50 has to be retarded with increasing $IMEP_g$ for each PRR. As expected, for a given $IMEP_g$, CA50 is retarded more at a lower PRR. It is remarkable that stable operation can be maintained for CA50 as late as 21°CA into the expansion stroke. (*i.e.* 381 °CA). At this late crank angle, the piston-expansion rate is high, as Fig. 7a shows. However, PRF80 has a comparatively high temperature-rise rate due to the presence of LTHR, and this enables stable autoignition despite the strong piston-expansion cooling [5].

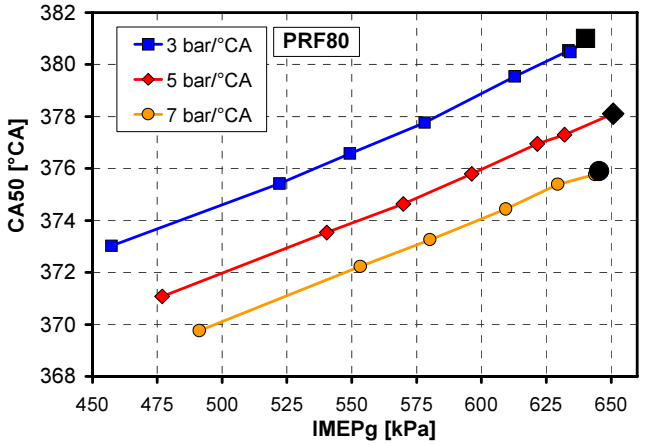

Figure 20. CA50 as a function of $IMEP_g$ for PRF80 operation with PRR = 3, 5 & 7 bar/°CA.

The larger black filled symbols in Fig. 20 represent the highest $IMEP_g$ for each PRR. As can be seen, operating with a PRR lower or higher than 5 bar/°CA does not offer any benefits in terms of maximum $IMEP_g$. In fact, rapid run-away occurs at a lower $IMEP_g$ for both the 3 and 7 bar/°CA data sets, as compared to the 5 bar/°CA data set. The reason for this will be explained below. First however, it is valuable to examine the potential influence of NO_x on the run-away for each PRR.

NO_x effect - Figure 21 plots the trapped in-cylinder NO_x mole fraction at intake valve closing (IVC) as a function of $IMEP_g$ for the three PRRs. The ppm numbers are computed based on the measured exhaust NO_x and the residual mole fraction[5]. Because of the high exhaust temperature at these high-load conditions, the residual mole fraction was low (on the order of 3.2%) for the highest $IMEP_g$ points. As can be seen, the NO_x emissions, and therefore also the trapped NO_x mole

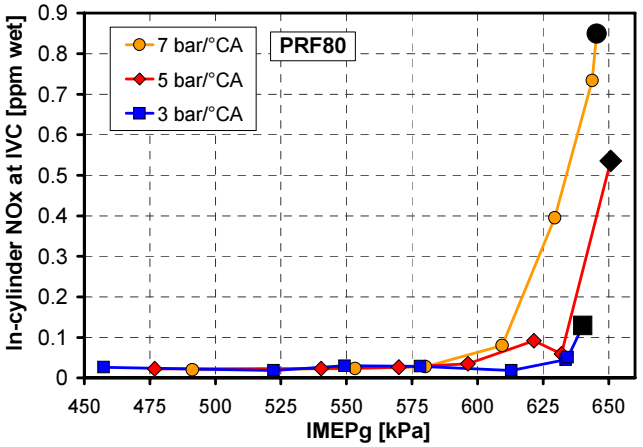

Figure 21. In-cylinder NO_x trapped at IVC as a function of $IMEP_g$ for PRF80 operation with PRR = 3, 5 & 7 bar/°CA.

[5] To estimate the amount of residuals, the residual temperature after exhaust blowdown was computed based on the measured cylinder pressure at exhaust valve opening (EVO), essentially using the equations presented in Ref. [20].

fraction is essentially zero for most of the $IMEP_g$ range for each PRR. However, for the highest $IMEP_g$ points, the trapped NO_x starts to increase rapidly. This indicates that the peak combustion temperatures at the control limit for each of the PRRs are just below the temperature where excessive NO_x will be produced. (Exhaust NO_x mole fraction is roughly 30 times higher than the trapped mole fraction.) This observation can help explain the rapid run-away observed for PRF80.

The main reason why operation at PRR = 3 bar/°CA reduces the maximum attainable $IMEP_g$ is that the more retarded CA50 reduces the thermal efficiency. To produce the same $IMEP_g$, the engine has to be operated with a slightly lower C/F ratio. This has consequences for the run-away that happens when the fueling is increased beyond the control limit. Figure 22 illustrates this. As can be seen, the run-away is very rapid once it commences. In this particular example, CA50 advances 10°CA in 2.3 s. (Compare to 10°CA in 10 s in Fig. 18, and 4°CA in 60 s in Fig. 12.) The PRR increases from 5 to 25 bar/°CA in the same time frame. This extremely rapid run-away rules out wall heating as a possible mechanism. Instead, it seems like a chemical mechanism has to be responsible. A more detailed examination provides further insights.

Figure 23 plots selected cycles from the run-away scenario shown in Fig. 22. Instead of labeling the cycles based on the time in s, they are labeled based on cycle #. Since there are 10 engine cycles per s at 1200 rpm, cycle #209 corresponds to 20.9 s, *etc*. As can be seen, the run-away leads to rapidly increasing PRR and extensive in-cylinder ringing. Along with the increased

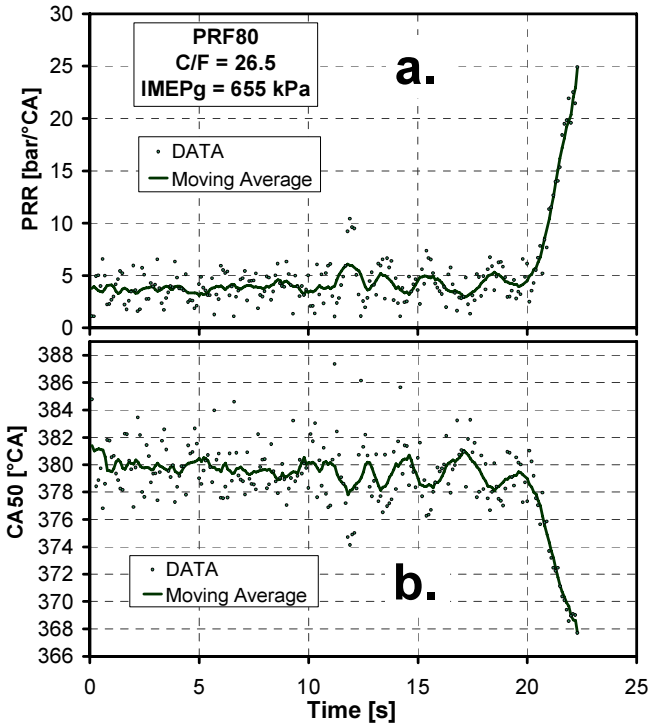

Figure 22. Very rapid run-away for PRF80 when operated with $IMEP_g$ beyond the control limit at PRR = 3 bar/°CA. 18.5% CSP.

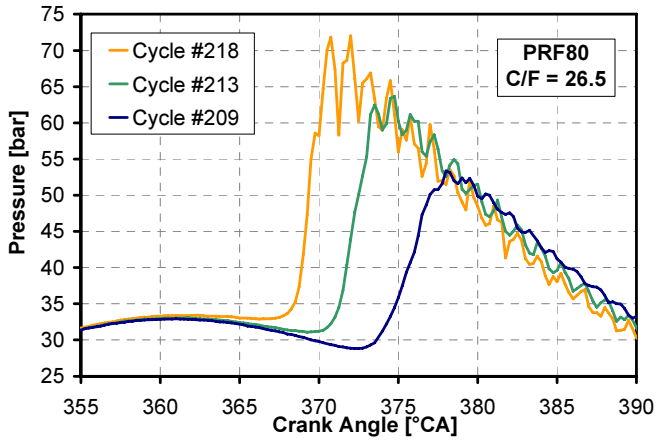

Figure 23. Selected pressure traces from the very rapid run-away scenario presented in Fig. 22.

peak pressures and more advanced CA50, the peak charge temperatures increase as well. This is shown in Fig. 24b. Before the very rapid run-away starts on cycle #201, the peak charge temperature is around 2000 K on average. Substantial but not excessive NO_x production can be expected during this period. However, during the run-away event, the peak charge temperature increases from around 2000 K to 2200 K. Based on the equations given in Ref. [13], this increase of the peak combustion temperature speeds up the thermal NO production rate by roughly a factor of 20. This could potentially provide a chemical mechanism for the very rapid run-away. However, is the autoignition for PRF80 sensitive to NO_x?

Indeed, measurements presented in the Appendix show that the autoignition of PRF80 exhibits a high sensitivity

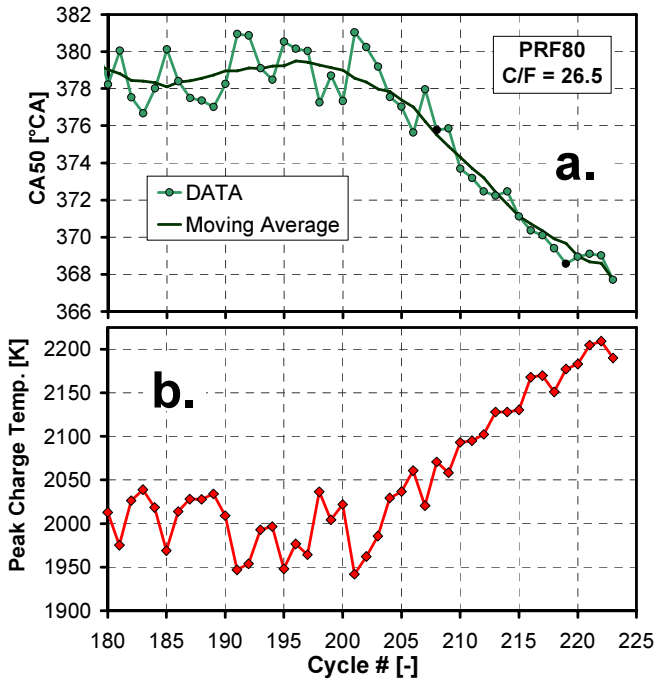

Figure 24. CA50 and peak combustion temperature during the very rapid run-away scenario presented in Figs. 22 and 23.

to NO_x. In fact, PRF80 has the highest sensitivity of the fuels tested. Figure A2 shows that adding 3.6 ppm NO_x to the intake advances CA50 by 4.6°CA. Furthermore, non-linear extrapolation of the data in Fig. A2 suggest that it would take 10 – 15 ppm NO_x to advance CA50 by 10°CA, which is the magnitude of the CA50 advance experienced during the run-away (see Fig. 24a). Given that the trapped in-cylinder NO_x just before run-away should be on the order of 1 ppm (compare Figs. 19, 21 & 24b) and that the NO_x production is expected to increase 20-fold during run-away, these facts provide a very strong case that the very rapid run-away for PRF80 is induced by NO_x. It is possible that changes to the concentration of other species also influence the autoignition. However, NO or NO_2 (NO_x) are the only species expected to increase rapidly with increased peak-combustion temperature, particularly in the 2000 – 2200 K range where the run-way was observed.

With this understanding of the NO_x-induced run-away, it is possible to explain the shift of the $IMEP_g$ limit with PRR, as shown earlier in Fig. 20. As can be seen, reducing the PRR from 5 to 3 bar/°CA lowers the maximum attainable $IMEP_g$ from 651 to 640 kPa. This happens because the thermal efficiency is lower with a more retarded CA50. Consequently, a lower C/F is required for the same $IMEP_g$. Also, cycle-to-cycle variations increase for a more retarded CA50. These circumstances together increase the risk for cycles with peak combustion temperature exceeding 2000 K, thus leading to rapid run-away for $IMEP_g$ slightly lower than for operation at 5 bar/°CA.

Furthermore, Fig. 20 shows that the maximum $IMEP_g$ is decreased also by increasing the PRR to 7 bar/°CA. This happens because the peak combustion temperatures increase with a more advanced CA50, thus increasing the risk for NO_x-induced run-away. The drop in maximum $IMEP_g$ is quite small (651 to 645 kPa) because the thermal efficiency increases somewhat with the more advanced CA50. Thus, lower fueling rates can be used for a given $IMEP_g$ and this limits the increase of the peak combustion temperatures when PRR is changed from 5 to 7 bar/°CA.

Chemically, the enhanced autoignition in the presence of NO_x has been attributed to the NO fraction of the NO_x, via two reactions [21]:

$$HO_2\bullet + NO = OH\bullet + NO_2 \quad (1)$$

$$RO_2\bullet + NO = RO\bullet + NO_2 \quad (2)$$

where R is an alkyl group and • marks a radical species. However, detailed treatment of this NO-enhanced autoignition chemistry is beyond the scope of the current study.

LOAD-LIMITING FACTOR FOR PRF60

Figure 8b shows that at PRR = 5 bar/°CA, PRF60 produces a slightly lower maximum $IMEP_g$ of 638 kPa compared to 651 kPa for PRF80. Furthermore, Fig. 8a shows that at high fueling rates, roughly 45% CSP is required to suppress the high reactivity of PRF60 and obtain a CA50 that results in a moderate PRR of 5 bar/°CA. In the following, the load-limiting factor for PRF60 is examined.

Because of the high CSP requirement, the intake O_2 mole fraction [O_2] decreases with fueling rate. This is shown in Fig. 25. At the highest load points, the intake [O_2] is reduced to 11.5%. Due to this reduction of [O_2], the actual ϕ increases faster with fueling for PRF60, compared to PRF80 and iso-octane. In fact, for the PRF60 data set at 5 bar/°CA, ϕ spans a wide range from 0.285 to 1.03[6]. In Fig. 26, the $IMEP_g$ is plotted against ϕ. From this graph, it is clear that the maximum $IMEP_g$ is achieved for stoichiometric operation. When the fueling is increased so that $\phi > 1$, the $IMEP_g$ starts to decrease. This occurs for two reasons. First, any fuel added for $\phi \geq 1$ does not increase the amount of heat release per unit charge mass since the combustion is limited by the inducted amount of O_2 [7]. On the other hand, the inducted mass of O_2 is reduced slightly with increasing ϕ since both increasing fuel and especially CSP reduce the charge [O_2]. Second, analysis of the data shows that both the volumetric efficiency and the thermodynamic cycle efficiency is reduced somewhat and these factors contribute to the lower $IMEP_g$.

As expected from combustion stoichiometry, the CO emissions increase rapidly for $\phi \geq 1$, as Fig. 27 shows.

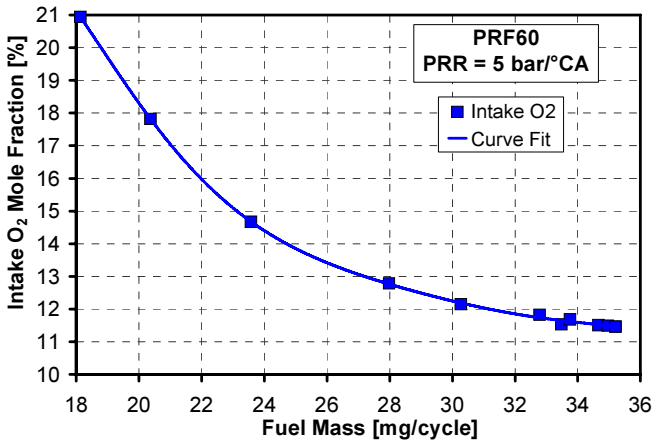

Figure 25. Intake [O_2] as a function of fueling rate for PRF60 with PRR = 5 bar/°CA.

[6] This can be compared to $0.382 \leq \phi \leq 0.493$ for iso-octane, and $0.376 \leq \phi \leq 0.676$ for PRF80, both at PRR = 5 bar/°CA.

[7] Chemkin computations show that, by the time of peak temperature, the cumulative heat release is somewhat greater for $\phi > 1.00$, but also that these richer cases have less exothermic CO – CO_2 recombination reactions during the expansion stroke. Therefore, effectively, the total heat release does not change in the $1.00 \leq \phi \leq 1.03$ range.

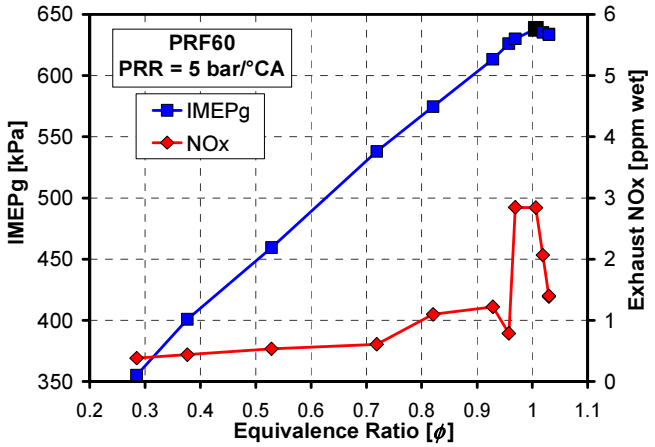

Figure 26. $IMEP_g$ and exhaust NO_x as a function of ϕ. PRF60 with PRR = 5 bar/°CA.

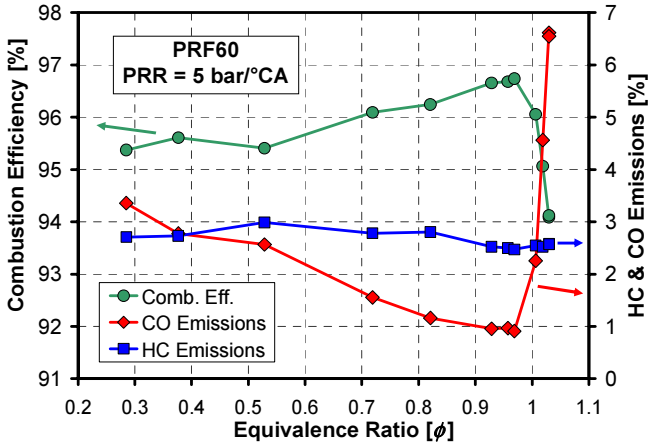

Figure 27. Combustion efficiency and CO emissions as a function of ϕ. PRF60 with PRR = 5 bar/°CA.

This happens because CO-to-CO_2 conversion is the last major combustion step [22,23], but there is not enough O_2 present for completion. On the other hand, HC does not rise for $\phi > 1$. This happens because all bulk-gas fuel breaks down despite $\phi > 1$. The nearly constant HC carbon fraction of 2.5-3 % stems from unburned HC from crevices [12,24].

Furthermore, Fig. 26 shows that the NO_x exhaust emissions are very low across the full fueling range. Even operation with $\phi \approx 1$ has very low NO_x. This happens because the high CSP fraction lowers the highest encountered peak combustion temperature to 1910 K due to the high heat capacity of CSP [18]. In addition, there is a very limited amount of O_2 available at the end of the combustion event for $\phi \geq 1$. These low NO_x emissions stand in contrast to the PRF80 data in Fig. 19, which showed that the NO_x emissions rise rapidly for the highest fueling rate. It was also concluded that excessive NO_x caused rapid run-away when the peak combustion temperature was allowed to rise above 2000 K (see Fig. 24b). Thus, the low NO_x emission for PRF60 can explain why run-away was not observed for PRF60.

Load limits at other PRRs for PRF60 – Figure 28 shows how CA50 has to be retarded with increasing $IMEP_g$ for each PRR. As expected, for a given $IMEP_g$, CA50 is retarded more at a lower PRR. The black filled symbols in Fig. 28 represent the highest IMEPg for each PRR. As can be seen, operating with PRR = 7 bar/°CA allows the $IMEP_g$ to be increased slightly from 638 to 643 kPa. This happens because slightly less CSP is required for operation with a higher PRR since CA50 is more advanced, so slightly more air is inducted.

On the other hand, more retarded operation with PRR = 3 bar/°CA reduces the maximum $IMEP_g$ somewhat to 620 kPa. This happens partly because the higher CSP fraction leads to a reduction of the available O_2, and partly because the more retarded CA50 leads to lower thermal efficiency. Figure 29 shows that thermal efficiency is substantially lower across the full range of $IMEP_g$. (The offset of the curves in the 450 – 600 kPa range provide a good measure of the effect of PRR/CA50 on the thermal efficiency. The rapid drop of thermal efficiency between 602 and 620 kPa for the 3 bar/°CA data set is caused mostly by the change of ϕ from 0.93 to 1.03 and the associated drop of combustion efficiency.)

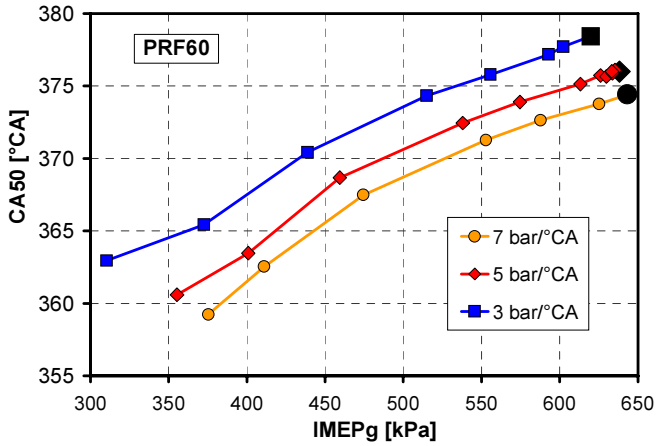

Figure 28. CA50 as a function of $IMEP_g$ for PRF60 operation with PRR = 3, 5 & 7 bar/°CA.

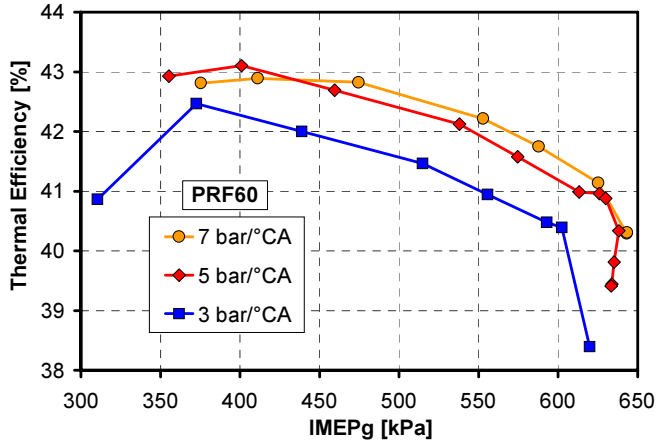

Figure 29. Thermal efficiency as a function of $IMEP_g$ for PRF60 operation with PRR = 3, 5 & 7 bar/°CA.

SUMMARY AND CONCLUSIONS

This experimental work examines how fuel autoignition reactivity affects the high-load limits of HCCI for naturally aspirated operation at 1200 rpm. This is done for three different fuels; iso-octane, PRF80, and PRF60.

For each operating point, the pressure-rise rate (PRR) was maintained at 3, 5, or 7 bar/°CA by carefully retarding the combustion phasing through adjustments of the intake temperature or EGR rate. The data show that the maximum attainable $IMEP_g$ is dependent on the fuel type, selected PRR, and CR. Figure 30 summarizes the findings. For each fuel with CR = 14 in Fig. 30, the PRR data set with the highest $IMEP_g$ is shown. In addition, iso-octane is plotted also for CR = 18 with a PRR of 5 bar/°CA.

This work identified five load-limiting factors, as annotated in Fig. 30 – from top to bottom:

1) Iso-octane at CR = 18:
   Wall-heating-induced run-away (T_{wall}).

2) PRF80 at CR = 14:
   NO_x-induced rapid run-away (NO_x)

3) PRF60 at CR = 14:
   EGR-induced oxygen deprivation (O_2)

4) Iso-octane at CR = 14:
   Excessive exhaust NO_x (Excessive NO_x).

5) Iso-octane at CR = 14 and a low PRR of 3 bar/°CA:
   Wandering unsteady combustion (Wandering CA50).

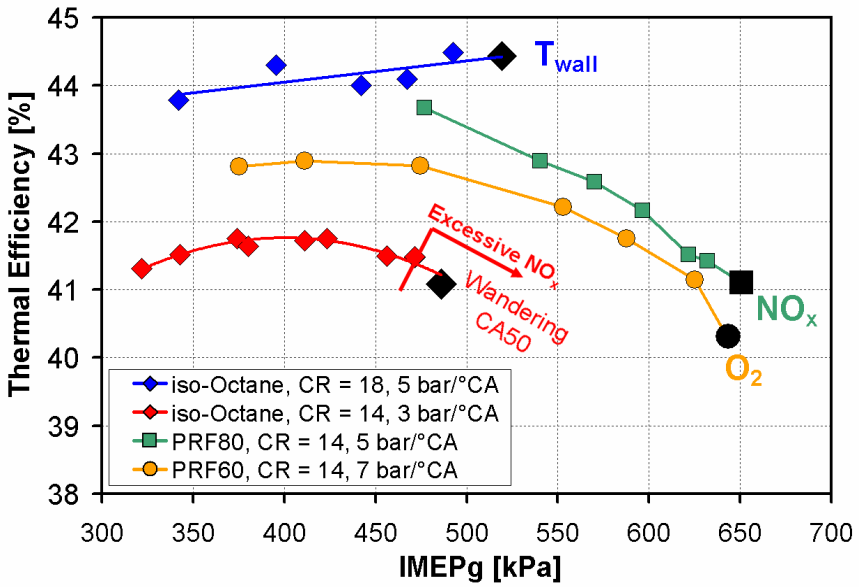

Figure 30. Summary graph showing thermal efficiency plotted against $IMEP_g$ for each fuel at the respective PRR which provides the highest $IMEP_g$. CR = 14, but iso-octane is also plotted for CR = 18. The load-limiting factor is indicated by the annotation - from top to bottom: Wall-heating-induced run-away, NO_x-induced rapid run-away, O_2-limited combustion, excessive exhaust NO_x, and wandering unsteady combustion.

For iso-octane, which has the highest resistance to autoignition of the fuels tested, the NO_x emissions become unacceptable before wall-heating-induced run-away happens (for PRR = 5 and 7 bar/°CA). The NO_x emissions for CR = 14 can be reduced by operation with a more retarded CA50 at a lower PRR of 3 bar/°CA. For such retarded operation, the high-load limit becomes less well defined since wall-heating-induced run-away does not occur. Instead, the high-load limit at $IMEP_g$ = 486 kPa becomes determined by wandering unsteady combustion with large cycle-to-cycle variations, as annotated in Fig. 30. Alternatively, the exhaust NO_x can be mitigated by operation with a higher CR, which allows operation with a lower ϕ for a given $IMEP_g$. The higher CR = 18 also increases the maximum $IMEP_g$ significantly to 520 kPa. The thermal efficiency is also increased significantly at the higher CR.

For a very reactive fuel like PRF60, large amounts of EGR are required to control the combustion phasing. Therefore, the maximum $IMEP_g$ becomes limited by the available oxygen since the EGR gases displace air. For such high-EGR operation, the highest $IMEP_g$ of 643 kPa was achieved for ϕ = 1.

A fuel of intermediate reactivity (PRF80) exhibits the highest $IMEP_g$ for the conditions of this study. For this fuel, the maximum $IMEP_g$ becomes limited to 651 kPa by NO_x-induced run-away. This happens because even small amounts of NO_x recycled via residuals or EGR enhance the autoignition sufficiently to advance the ignition point. This leads to higher peak-combustion temperatures and more NO_x formation, thus making a rapid run-away situation inevitable.

Overall, the two-stage ignition fuels PRF80 and PRF60 produced higher $IMEP_g$. This happens mostly because the higher autoignition reactivity allows operation with lower T_{in}, so more gas mass can be inducted for each cycle. The two-stage ignition fuels also allow a combination of more retarded CA50 and lower C/F mass ratio.

Finally, it can be noted from the slopes of the PRF80 and PRF60 curves in Fig. 30, that the need to use extensive CA50 retard at the highest loads leads to a small but significant efficiency penalty. Techniques such as partial fuel stratification [11] or enhanced thermal stratification [10,14,16] can allow operation with more advanced CA50, and therefore have potential to increase both the maximum $IMEP_g$ and provide higher thermal efficiencies.

ACKNOWLEDGEMENTS

The authors would like to thank Kenneth St. Hilaire, Eldon Porter and Gary Hubbard for their dedicated support of the HCCI laboratory.

Financial support for this investigation was provided by Aramco Services Company under WFO contract 083041026.

The work was performed at the Combustion Research Facility, Sandia National Laboratories, Livermore, CA. Financial support for establishing and operating the HCCI lab facility was provided by the U.S. Department of Energy, Office of FreedomCAR and Vehicle Technologies. Sandia is a multiprogram laboratory operated by the Sandia Corporation, a Lockheed Martin Company, for the United States Department of Energy's National Nuclear Security Administration under contract DE-AC04-94AL85000.

REFERENCES

1. Risberg, P., Kalghatgi, G., and Ångström, H.-E., "Auto-Ignition Quality of Gasoline-Like Fuels in HCCI Engines", SAE Paper 2003-01-3215, 2003.

2. Christensen, M., Johansson, B., Amnéus, P., and Mauss, F., "Supercharged Homogeneous Charge Compression Ignition", SAE Paper 980787, 1998.

3. Yao, M., Chen, Z., Zheng, Z., Zhang, B., and Xing, Y., "Effects of EGR on HCCI Combustion Fuelled with Dimethyl Ether (DME) and Methanol Dual-Fuels", SAE Paper 2005-01-3730, 2005.

4. Risberg, P., Kalghatgi, G., Ångström, H.-E., and Wåhlin, F., "Auto-Ignition Quality of Diesel-Like Fuels in HCCI Engines", SAE Paper 2005-01-2127, 2005.

5. Sjöberg, M. and Dec, J.E., "Comparing Late-cycle Autoignition Stability for Single- and Two-Stage Ignition Fuels in HCCI Engines", Proceedings of the Combustion Institute, Vol. 31, pp. 2895–2902, 2007.

6. Sjöberg, M. and Dec, J.E., "EGR and Intake Boost for Managing HCCI Low-Temperature Heat Release over Wide Ranges of Engine Speed", SAE Paper 2007-01-0051, 2007.

7. Olsson, J.-O., Tunestål, P., Johansson, B., Fiveland, S., Agama, J.R., and Assanis, D.N., "Compression Ratio Influence on Maximum Load of a Natural Gas-Fueled HCCI Engine", SAE Paper 2002-01-0111, 2002.

8. Christensen, M., Hultqvist, A., and Johansson, B., "Demonstrating the Multi Fuel Capability of a Homogeneous Charge Compression Ignition Engine with Variable Compression Ratio", SAE Paper 1999-01-3679, 1999.

9. Urushihara, T., Hiraya, K., Kakuhou, A., and Itoh, T., "Parametric Study of Gasoline HCCI with Various Compression Ratios, Intake Pressures and Temperatures", A New Generation of Engine Combustion Processes for the Future?, pp. 77 - 84, Paris, 2001.

10. Sjöberg, M., Dec, J.E., Babajimopoulos, A., and Assanis, D., "Comparing Enhanced Natural Thermal Stratification against Retarded Combustion Phasing for Smoothing of HCCI Heat-Release Rates", SAE Paper 2004-01-2994, 2004.

11. Sjöberg, M. and Dec, J.E., "Smoothing HCCI Heat-Release Rates using Partial Fuel Stratification with Two-Stage Ignition Fuels", SAE Paper 2006-01-0629, 2006.

12. Dec, J.E. and Sjöberg, M., "A Parametric Study of HCCI Combustion – the Sources of Emissions at Low Loads and the Effects of GDI Fuel Injection", SAE Paper 2003-01-0752, 2003.

13. Heywood, J. B., Internal Combustion Engine Fundamentals, McGraw-Hill, New York, 1988.

14. Sjöberg, M. and Dec, J.E., "Effects of Engine Speed, Fueling Rate, and Combustion Phasing on the Thermal Stratification Required to Limit HCCI Knocking Intensity", SAE Paper 2005-01-2125, 2005.

15. Eng, J.A., "Characterization of Pressure Waves in HCCI Combustion", SAE Paper 2002-01-2859, 2002.

16. Sjöberg, M., Dec, J.E., and Cernansky, N.P., "Potential of Thermal Stratification and Combustion Retard for Reducing Pressure-Rise Rates in HCCI Engines, based on Multi-Zone Modeling and Experiments", SAE Paper 2005-01-0113, 2005.

17. Tsurushima, T., Kunishima, E., Asaumi Y., Aoyagi, Y., and Enomoto, Y., "The Effect of Knock on Heat Loss in Homogeneous Charge Compression Ignition Engines", SAE Paper 2002-01-0108, 2002.

18. Sjöberg, M., Dec, J.E., and Hwang, W., "Thermodynamic and Chemical Effects of EGR and Its Constituents on HCCI Autoignition", SAE Paper 2007-01-0207, 2007.

19. Sjöberg, M. and Dec, J.E., "Combined Effects of Fuel-type and Engine Speed on Intake Temperature Requirements and Completeness of Bulk Gas Reactions in an HCCI Engine", SAE Paper 2003-01-3173, 2003.

20. Sjöberg, M. and Dec, J.E., "An Investigation of the Relationship between Measured Intake Temperature, BDC Temperature, and Combustion Phasing for Premixed and DI HCCI Engines", SAE Paper 2004-01-1900, 2004.

21. Risberg, P., Johansson, D., Andrae, J., Kalghatgi, G., Björnbom, P., and Ångström, H.-E., "The Influence of NO on the Combustion Phasing in an HCCI Engine", SAE Paper 2006-01-0416, 2006.

22. Dec, J. E., “A Computational Study of the Effects of Low Fuel Loading and EGR on Heat Release Rates and Combustion Limits in HCCI Engines,” SAE Paper 2002-01-1309, 2002.

23. Sjöberg, M. and Dec, J. E., “An investigation into lowest acceptable combustion temperatures for hydrocarbon fuels in HCCI engines,” Proc. Combust. Inst., Vol. 30, pp. 2719 – 2726, 2005.

24. Aceves S.M., Flowers, D.L., Espinosa-Loza, F., Martinez-Frias, J., Dec, J.E., Sjöberg, M., Dibble R.W., and Hessel, R.P., “Spatial Analysis of Emissions Sources for HCCI Combustion at Low Loads Using a Multi-Zone Model”, SAE Paper 2004-01-1910, 2004.

25. De Zilwa, S. and Steeper, R., “Predicting NO_X Emissions from HCCI Engines Using LIF Imaging,” SAE paper 2006-01-0025, 2006.

26. Dubreuil, A., Foucher, F., Mounaim-Rousselle, C., “Effect of Chemical Components, Amount and Temperature of the Exhaust-Gas-Recirculation on the Combustion Development in HCCI Mode”, Proceeding of THIESEL 2006, pp. 629 – 631, 2006.

27. Mehl, M., Tardani, A., Faravelli, T., Ranzi, E., Errico, G.D’, Lucchini, T., Onorati, A., Miller, D., and Cernansky, N, “A Multizone Approach to the Detailed Kinetic Modeling of HCCI Combustion”, SAE-NA paper 2007-24-0086, 2007.

28. Prabhu, S.K., Li, H., Miller, D.L., Cernansky., N.P., “The Effect of Nitric Oxide on Autoignition of a Primary Reference Fuel Blend in a Motored Engine”, SAE paper 932757, 1993

APPENDIX: CA50 SENSITIVITY TO INTAKE NO_x

To guide the interpretation of the observed load limits, the sensitivity of CA50 to the trapped mole fraction of NO_x was measured. Since NO_x seeding using gas bottles with NO_x was not available, the NO_x was produced "on-the-fly" by operation with fuel stratification. The fuel stratification raised the local ϕ, and the associated higher combustion temperatures increased the NO_x production [12,25]. By varying the start of injection (SOI), the degree of stratification, and hence the amount of NO_x, could be varied. Some of this exhaust NO_x was then recycled back into the intake via the pipe equipped with an EGR cooler, as shown in Fig. 1. This kind of fuel-stratified combustion was performed using an alternate-fire mode of operation, as illustrated in Fig. A1. The sequence repeated continuously, so cycle #1 followed after cycle #8. As can be seen, cycle #2 produced the NO_x by using a late SOI, while the other 7 cycles were well-mixed with fuel injection during the early part of the intake stroke (SOI = 40°CA). In fact, for all cycles, 75% of the fuel was provided using the external fuel vaporizer and only 25% of the fuel was introduced via direct injection. This ensured a high degree of homogeneity for cycle #1 and reduced the effect of fuel vaporization. The data were acquired only on cycle #1 for at least 40 consecutive 8-cycle sequences.

To trap controlled amounts of NO_x for cycle #1, the engine was operated with a fixed EGR rate for each fuel. In this way, the trapped [NO_x] could be computed based on the measured exhaust [NO_x], the EGR rate, and the computed trapped mole fraction of fresh gases (~95%). By having six well-mixed "purge" cycles before cycle #1, the data analysis is simplified since it can be assumed that the well-mixed cycles produced no NO_x at the fueling rates investigated here. Hence, all trapped NO_x stemmed from the EGR with no additional contribution from trapped residuals. (For example, it is more complicated to accurately compute the trapped [NO_x] for cycles #3 and #4 since varying amounts of residual NO_x add to the inducted NO_x.)

Figure A2 shows that the autoignition is enhanced for all three fuel investigated here. PRF80 has an especially high sensitivity to NO_x addition. One reason for this is that the amount of LTHR increases particularly quickly with NO_x addition for PRF80.

The enhancement of HCCI autoignition for two-stage ignition fuels by NO addition has been observed experimentally by both Risberg *et al.* [21] and Dubreuil *et al.* [26]. Among the fuels examined by Risberg *et al.,* PRF84 is the fuel with composition most similar to PRF80 studied here. Their measured sensitivity for PRF84 to addition of only a few ppm NO_x was not quite as high as found here. The higher sensitivity shown in

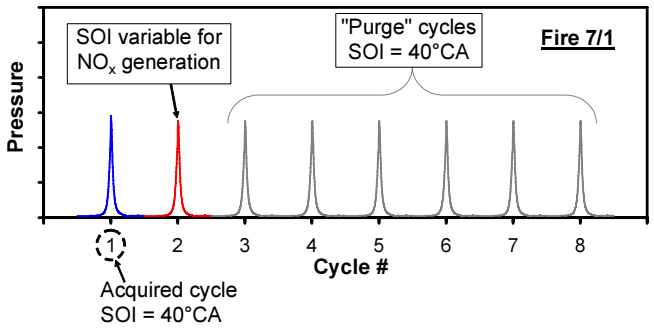

Figure A1. Alternate-fire sequence for measurement of CA50 sensitivity to NO_x. The NO_x is produced by stratification on cycle #2 and recirculated to the intake using EGR.

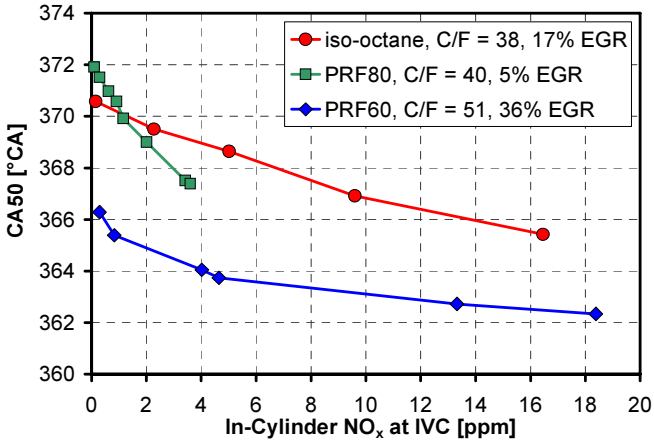

Figure A2. CA50 as a function of trapped [NO_x] at IVC for iso-octane, PRF80, and PRF60. T_{in} = 187°C for iso-octane, and T_{in} = 60°C for PRF80 & PRF60.

Fig. A2 can be attributed to the more retarded CA50 of the current study. Furthermore, based on their findings for PRF84, it could be expected that for PRF80, the enhancing effect of NO_x reaches a maximum around 20 – 50 ppm and that even higher concentrations of NO_x would lead to retarding CA50. Given the trends in Fig. A2, such a scenario appears consistent with the current data. Based on this, it can be speculated that the rapid CA50 run-away shown in Fig. 22 would have eventually slowed down if more data with even higher peak combustion temperatures and more NO_x generation had been acquired.

Furthermore, it can be noted that recent HCCI multi-zone modeling of iso-octane combustion has shown that about 8 ppm of NO present during the compression stroke advances CA50 by a couple of °CA [27]. This sensitivity is in approximate agreement with the iso-octane data in Fig. A2. Finally, these results from HCCI experiments are in general agreement with a previous study of the enhancing effect of NO on the autoignition in the end gas of an SI engine fueled with PRF87 [28].